CZECH TECHNICAL UNIVERSITY
IN PRAGUE

Faculty of Nuclear Sciences and Physical Engineering

Department of Physics

Bachelor Thesis

Study of Thermonuclear Plasma Using Semiconductor Detectors

Peter Švihra

Supervisor: Ing. Michal Marčišovský

Consultant: Ing. Martin Hejtmánek

Prague, 2015

ČESKÉ VYSOKÉ UČENÍ TECHNICKÉ
V PRAZE
Fakulta Jaderná a Fyzikálně Inženýrská
Katedra fyziky

Bakalářská práce

Studium termojaderného plazmatu polovodičovými detektory

Peter Švihra

Vedoucí práce: Ing. Michal Marčišovský

Konzultant: Ing. Martin Hejtmánek

Praha, 2015

Na toto místo přijde svázat **zadání bakalářské práce**!
V jednom z výtisků musí být **originál** zadání, v ostatních kopie.

Declaration

I hereby declare, that I've written this thesis by myself and I've used only the materials stated in the references section.

I have no reason to object to use this work according to the section 60 of Act No. 121/2000 Coll.,On Copyright, on Rights Related to Copyright, and on Change of Some Acts (Copyright Act)

Prague, date ....

Peter Švihra

Acknowledgement

I would like to express my gratitude to everyone who supported me during the creation of this work. I am very grateful to my supervisor Ing. Michal Marčišovský and to my consultant Ing. Martin Hejtmánek for their patience, willingness and professional assistance during writing this thesis. My thanks also belong to Ing. Jakub Cikhardt for his help with operating the plasma focus PFZ–200.

Thesis title:
Study of Thermonuclear Plasma Using Semiconductor Detectors

Author: Peter Švihra

Field of study: Physics and Technology of Thermonuclear Fusion

Thesis type: Bachelor thesis

Supervisor: Ing. Michal Marčišovský

Consultant: Ing. Martin Hejtmánek

Abstract:
Plasma physics and thermonuclear fusion provide a promising route to a new reliable energy source. This thesis investigates properties of plasma behaviour using semiconductor pixel detectors. These detector systems are well understood as semiconductor trackers have been extensively employed in particle physics.

Plasma is a quasi–neutral state of matter that exhibits collective behaviour. Thermonuclear fusion occurs when dense plasma is heated to high temperatures. The reaction between light nuclei releases excessive binding energy. Currently, a number of experiments using magnetic or inertial confinement are being developed as tools for harvesting this energy.

Possibility of investigation of plasma properties is to some extent determined by the choice of detectors of the plasma burst products. The theoretical part of this thesis covers processes of interaction of ionizing radiation with matter. The relevant characteristics of semiconductor detectors are explored in detail. Designing a new diagnostic method consists of three phases: simulation, construction and measurement. Design characteristics of PFZ-200 plasma focus and Medipix2, Timepix semiconductor pixel detectors are given. The results from the measurement show that employing this approach provides new opportunities of plasma diagnostics. However, a comparison to other methods and threshold energy specification is advised for suitable interpretation.

Keywords: thermonuclear fusion, plasma focus PFZ-200, Medipix2 MXR, Timepix, silicon particle detector

Název práce:
Studium termojaderného plazmatu polovodičovými detektory

Autor: Peter Švihra

Obor: Fyzika a technika termojaderné fúze

Druh práce: Bakalářská práce

Vedoucí práce: Ing. Michal Marčišovský

Konzultant: Ing. Martin Hejtmánek

Abstrakt:
Fyzika plazmatu a termonukleární fúze poskytuje slibnou cestu k novému a spolehlivému zdroji energie. Tato práce zkoumá vlastnosti plazmatu pomocí polovodičových pixelových detektorů. Problematika polovodičových senzorů je velmi dobře známa především pro jejich použití v částicové fyzice.

Plazma je kvazineutrální skupenství hmoty vykazující kolektivné chování. Termonukleární fúze nastává, když je husté plazma zahřáto na vysokou teplotu. Tato reakce mezi dvěma atomy lehkých jader uvolňuje přebytečnou vazebnou energii. V současnosti je vyvíjeno velké množství experimentů používajících magnetické nebo inerciální udržení jako nástrojů určených k získávání této energie.

Možnost zkoumání vlastností plazmatu je v jisté míře určena volbou detektorů plazmových výbuchů. Teoretická část této práce pokrývá procesy interakce ionizujícího záření s látkou. Důležité vlastnosti polovodičových detektorů jsou do detailů prozkoumány. Návrh nové diagnostické metody sestává ze tří fází: simulace, konstrukce a měření. Uvedeny jsou rovněž konstrukční parametry plazma fokusu PFZ-200 a polovodičových pixelových detektorů Medipix2 a Timepix. Výsledky měření poukazují, že použití této metody poskytuje nové možnosti diagnostiky plazmatu. Avšak, pro vhodnou interpretaci je doporučeno porovnání s jinými metodami a stanovení prahové energie.

Klíčová slova: termojaderná fúze, plazma fokus PFZ-200, Medipix2 MXR, Timepix, křemíkový detektor částic

Contents

List of Figures

Introduction

Currently, the annual world primary energy consumption is enormous, roughly 540 EJ. Given these conditions, it is expected that fossil fuels will be exhausted within a couple of decades [1]. Renewable energy sources, e.g. sunlight and wind, have yet to prove their dependability, while fission is considered dangerous due to a possibility of nuclear and radiation accidents. This situation could be resolved by developing a reliable and stable source of energy such as thermonuclear fusion.

Fusion of atoms is a process which requires relatively high initial energies, and even under these conditions happens with a low probability. This probability can be enhanced by achieving fusion in plasma where cross–section of the reaction is large. Although scientists have already managed to execute an operational thermonuclear reaction, many theoretical and technological challenges have to be overcome before thermonuclear power can be efficiently harvested. There are two major engineering problems: heating and containment of plasma.

This thesis studies a new diagnostic method in plasma research which uses semiconductor pixel detectors, which are widely employed in particle physics. It focuses on theoretical understanding, numerical simulations, construction of the apparatus and performing measurements.

Plasma is a quasi–neutral state of matter that exhibits collective behaviour. Thermonuclear fusion occurs when dense plasma is heated to high temperatures. This reaction between nuclei of light atoms releases excessive binding energy. Currently, the number of experiments using magnetic or inertial confinement are being developed as the means of harvesting this energy.

In the first chapter, basic characteristics of plasma are given along with experiments using magnetic and inertial fusion. A substantial part is reserved for a detailed description of magnetic pinch and plasma focus. The second chapter is devoted to types and occurrence of plasma instabilities. Principles of particle detection, mainly in semiconductors, together with a general description of interactions of ionizing radiation with matter is given in the third chapter.

The fourth chapter deals with the design characteristics and optical diagnostics systems of PFZ-200 plasma focus device which was the source of the studied plasma. The chapter also describes Medipix2 and Timepix pixel detectors and lists their parameters. These detector systems provide the basis of the proposed observation method. Characteristics of Geant4 simulation toolkit are included as well.

Finally, the fifth chapter describes the results of simulations, the process of creation of the operating apparatus and the data acquired from measurements. A comprehensive summary of this work and its results is given in the conclusions.

Chapter 1

Plasma Physics and Experiments

According to the latest data of the Planck Collaboration, only about 4.9% of our universe is composed of atomic matter. Moreover, approximately 99% of it, including stars, nebulae and intergalactic space, are made of plasma. The corresponding pie chart is shown in figure (1.1). Plasma is a quasi–neutral state of matter showing collective behaviour, i.e. it consists of positively charged ions and negative electrons, thus appearing quasi–neutral. However, it creates and interacts with electromagnetic field.

The examples of naturally occurring plasma on our planet are aurora and lightning, it can also be found in ionosphere. Man–made plasma can be utilised in a variety of technologies such as lighting, cutting, deposition of layers of atoms on materials, or as a mean to extract energy in controlled thermonuclear fusion.

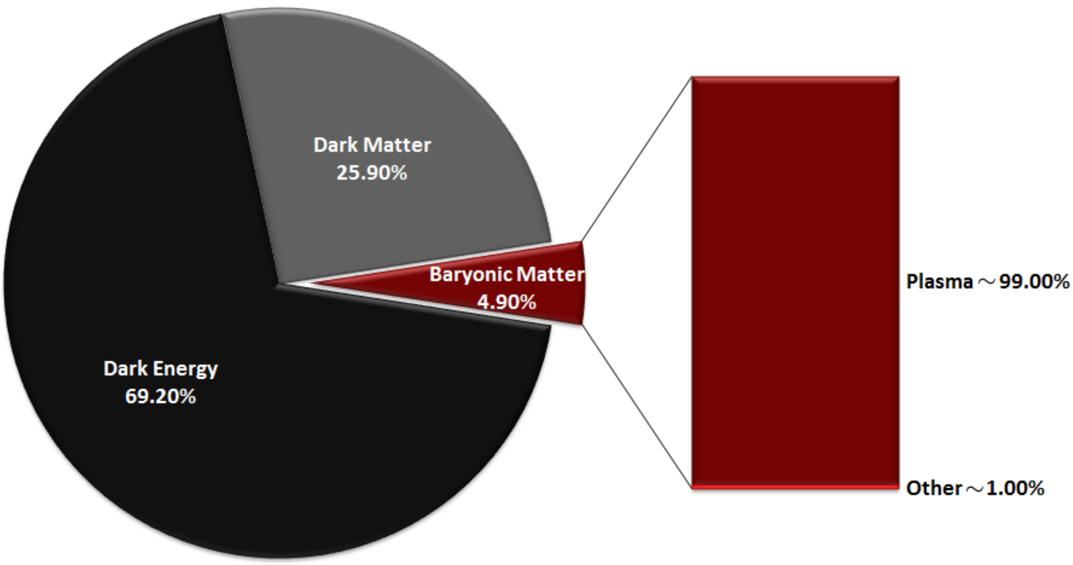

Figure 1.1: Distribution of matter and energy in the universe. Only 4.90% of our universe is created from baryonic matter, of which about 99.00% is ionized. [2]

1.1 Thermonuclear fusion

Thermonuclear fusion is a reaction between the nuclei of light atoms that releases energy. By fusing atoms whose mass number is lower than iron's, more stable elements can be acquired, along with the release of excessive energy matching the differences of binding energies, as shown in figure (1.2). Depending on the type of reaction, this energy can be released in the form of creation of energetic particles such as positron and neutrino, neutron, gamma photon or alpha particle. Part of the energy is also carried away as kinetic energy by a newly formed atom. For comparison, for the same masses of hydrogen and uranium isotopes, the energy obtained from fusion is about 3 to 4 times larger than the one obtained by fission.

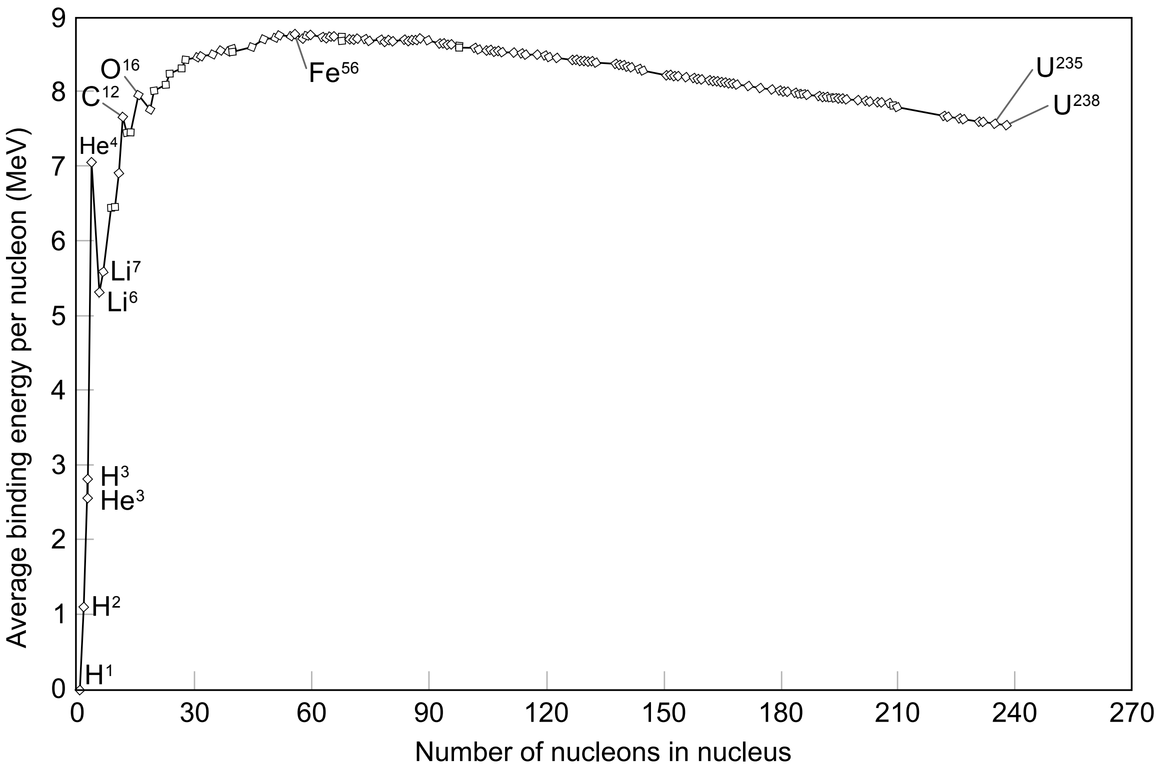

Figure 1.2: Average binding energy (energy needed to disassemble an atomic core) per nucleon in MeV against number of nucleons in nucleus. Important elements for nuclear fusion and fission are highlighted. ^{56}Fe is an element from which no energy can be released neither by fission or fusion. [3]

Theoretically, any two nuclei can be combined. Although it has been observed that the main fusion processes in the Sun are proton–proton (PP) chain, carbon–nitrogen–oxygen (CNO) cycle and later on in the life of the Sun triple–alpha process. In the PP chain, an alpha particle and 2 atoms of hydrogen are created via three–stepped mechanism, from 6 hydrogen atoms altogether. In the CNO cycle, helium is made during change of carbon to oxygen to nitrogen back to carbon, using 4 hydrogen atoms. At the end of the life of the Sun, triple–alpha process will create atoms of carbon using 3 atoms of helium with sub–step of creating atom of beryllium $^8_4$Be.

In the stars, the plasma is burning (self–containing fusion) because of the high temperatures $T \approx 15 \cdot 10^6$ K in the stellar core and an enormous gravitational pressure, binding the atoms in a gravitational potential well. However, in laboratory conditions, such plasma parameters are beyond humanity's technological reach. Therefore the most promising reactions are D–D (deuterium–deuterium)

$$
\begin{aligned}
{}_1\mathrm{D}^2 + {}_1\mathrm{D}^2 &\longrightarrow {}_2\mathrm{He}^3 + {}_0\mathrm{n}^1 \quad (3.3\ \mathrm{MeV}) \\
{}_1\mathrm{D}^2 + {}_1\mathrm{D}^2 &\longrightarrow {}_1\mathrm{T}^3 + {}_1\mathrm{H}^1 \quad (4.0\ \mathrm{MeV})
\end{aligned}
$$

and most importantly D–T (deuterium–tritium)

$$
{}_1\mathrm{D}^2 + {}_1\mathrm{T}^3 \longrightarrow {}_2\mathrm{He}^4 + {}_0\mathrm{n}^1 \quad (17.6\ \mathrm{MeV})
$$

where the numbers in the brackets are total energy yields. The probability of these reactions is sufficient for energies of the order of 10 keV. It falls within the Gamow peak region, which is a product of Maxwell–Boltzman energy distribution of particles and quantum tunnelling probability through the nuclear Coulombic barrier [4]. The fusion cross–section σ can be calculated as

$$
\sigma(E) = \frac{S(E)}{E} \exp\left(-\sqrt{\frac{E_G}{E}}\right), \tag{1.1.1}
$$

where E is energy of an incident particle, $S(E)$ is probability of the reaction without Coulombic barrier (dependant on E only for compound nuclei), the exponential represents probability of quantum tunnelling. E_G is Gamow energy defined as

$$
E_G = 2\mu c^2 \left(\pi \frac{e^2}{\hbar c} Z_1 Z_2\right), \tag{1.1.2}
$$

for Z_1 and Z_2 atomic numbers of reacting nuclei, μ reduced mass, c speed of light, e elementary charge and $\hbar$ reduced Planck constant.

Reaction rate $\langle \sigma v \rangle$ is only a function of plasma temperature T. It can be written as

$$
\langle \sigma v \rangle = \int_{-\infty}^{\infty} \sigma(v) v f(v) \, \mathrm{d}v, \tag{1.1.3}
$$

which, considering (1.1.1) and Maxwell–Boltzman distribution $f(v)$, leads to

$$
\langle \sigma v \rangle = \sqrt{\frac{2}{\pi \mu}} \left(\frac{1}{k_B T}\right)^{3/2} \int_0^{\infty} S(E) \exp\left(-\frac{E}{k_B T} - \sqrt{\frac{E_G}{E}}\right) \mathrm{d}E, \tag{1.1.4}
$$

where v is a relative velocity of the colliding particles and k_B is Boltzmann constant. The cross–section and reaction rate dependency on energy is shown in figure (1.4).

In addition, the plasma also loses its energy via bremsstrahlung, black body radiation or due to the interaction with surrounding containment wall. In order to create plasma which generates more energy than consumes, the Lawson's criterion (1.1.5) must be satisfied.

$$
n\tau \geq \frac{3 k_B T}{\frac{\eta}{4(1-\eta)} \langle \sigma v \rangle \Delta E - \alpha T^{\frac{1}{2}}}, \tag{1.1.5}
$$

where n is the density of plasma, τ is containment time, η is the efficiency factor, ΔE is the total energy output and α is a constant related to the radiation power loss. For D–T fusion, the Lawson's criterion is $n\tau \geq 10^{14}$ cm^{-3}s. [6]

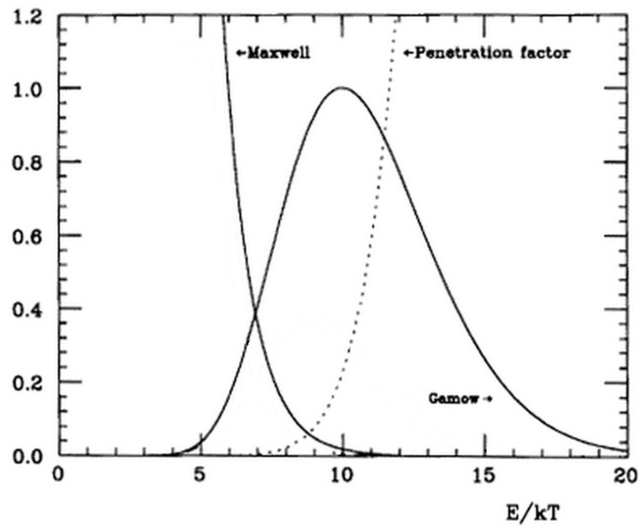

Figure 1.3: Gamow peak for the Maxwellian distribution (solid curve), normalized to 400 at $E/kT = 0$. The dotted curve is a penetration factor, representing the quantum tunnelling probability of nuclei. Gamow peak is a product of the distribution and penetration factor. [4]

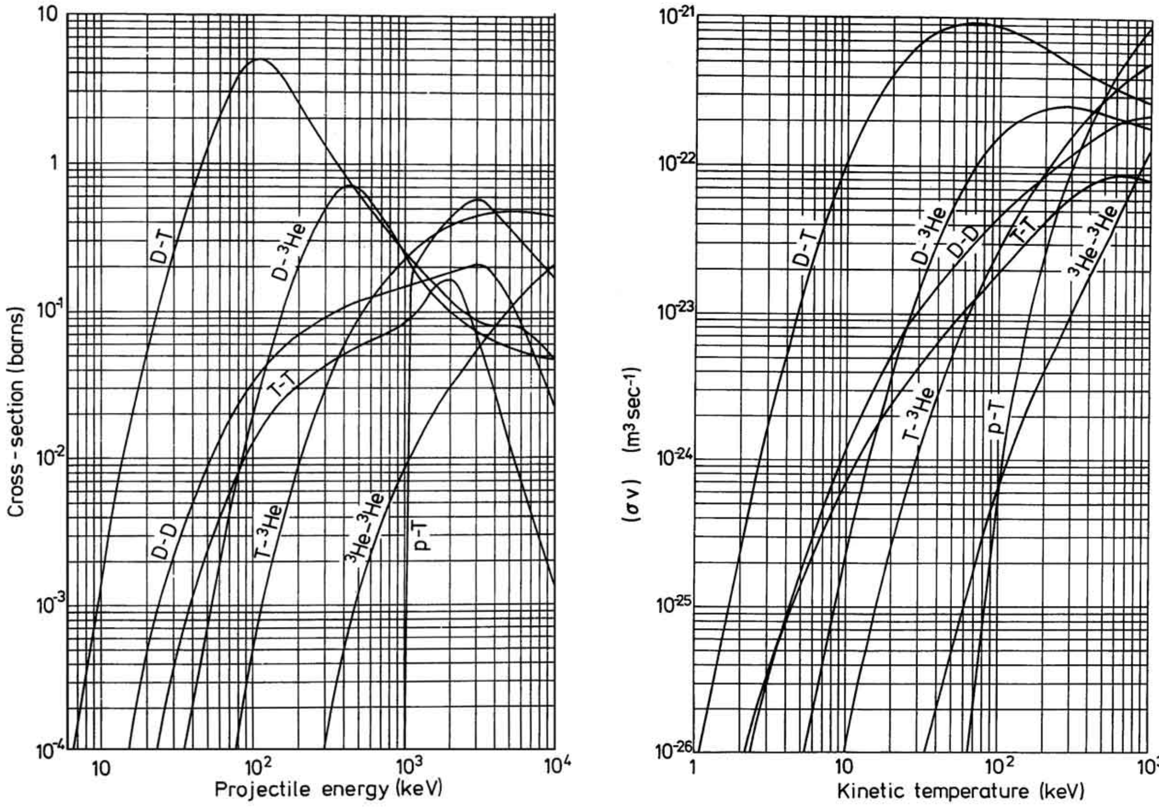

(a) Nuclear fusion cross-section σ as a function of incident particle energy, for D–D, D–T, D–^{3}He, T–T, ^{3}He–^{3}He and p–T reactions.

(b) Nuclear fusion reactivity $\langle \sigma v \rangle$ as a function of kinetic temperature, for D–D, D–T, D–^{3}He, T–T, ^{3}He–^{3}He and p–T reactions.

Figure 1.4: Cross–section and reactivity of selected fusion reactions as a function of kinetic energy and temperature. [5]

1.2 Experiments

There are several approaches of studying plasma and fusion in particular. According to the Lawson's criterion, with a large confinement time τ, plasma density n can be smaller and vice–versa. These boundary values can be achieved in magnetic ($n \sim 10^{14}$ cm^{-3}, $\tau \sim 1$ s), respectively inertial confinement ($n \sim 10^{23}$ cm^{-3}, $\tau \sim 10^{-9}$ s). Fusion experiments with low plasma density such as tokamaks, spheromaks and stellarators belong to the magnetic confinement category, whereas inertial fusion belongs to the inertial confinement. Experiments with pinches and plasma foci fit with their parameters ($n \sim 10^{18}$ cm^{-3}, $\tau \sim 10^{-4}$ s) somewhere in between.

1.2.1 Tokamak

Tokamaks (from Russian *тороидальная камера с магнитными катушками* – toroidal chamber with magnetic coils) are using electromagnetic induction, microwaves, accelerated neutral atoms or their combination to heat and ionize gas. Simultaneously, the magnetic field generated by the coils around the toroidally–shaped chamber together with the field created by electric current are containing plasma in the toroid. For a DT reaction, atoms of the produced helium are used to reheat the fuel and neutrons are absorbed by the reactor wall. For a typical tokamak plasma density, the containment time falls within the range of a few seconds, according to the Lawson's criterion. [6]

Various problems occur while trying to achieve commercial fusion in the tokamak devices. The fuel is not dense enough, the electrons and ions are drifting into the chamber walls or the size of the tokamak is not sufficient, hence not able to generate more power than it consumes. These losses are included in the fusion energy gain factor Q, defined as

$$Q = \frac{P_f}{P_h}, \tag{1.2.1}$$

where P_f is the power extracted from fusion reactions and P_h is the power required for the plasma heating. Upon reaching $Q = 1$, the so–called break–even occurs.

Currently, the largest experiment, called ITER, (from Latin *iter* – direction, way) is being built in Cadarache, France. It is a successor to JET (Joint European Torus), a tokamak in Oxfordshire, UK, which was the first to achieve a controlled release of fusion power. ITER is expected to be the first tokamak able to reach Q factor of 10.

1.2.2 Inertial fusion

Inertial fusion is initiated either by heating and compressing the targeted fuel pellet using high–power laser beams or by strong electrostatic field. The confinement times are therefore smaller by many orders of magnitude than in tokamaks.

Using high–power lasers, the compressed atoms undergo process of thermonuclear fusion, followed by a rapid expansion. The compression is achieved by ablation – the pellet is evenly irradiated by laser beams or surrounded by a hohlraum (from German *hohlraum* – cavity), to which the beams enter and subsequently generate X–rays [6]. The comparison of the processes is shown in figure (1.5).

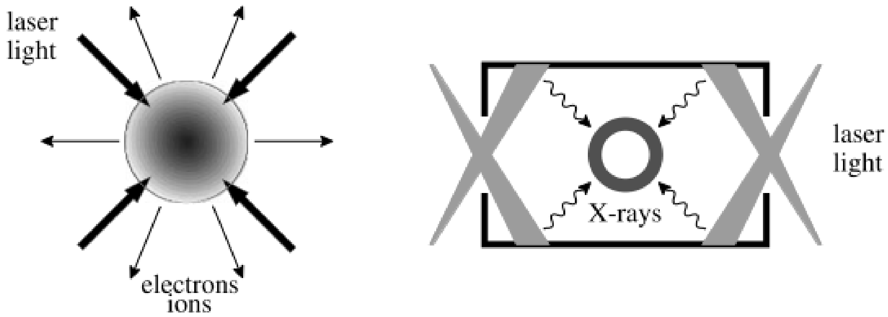

Figure 1.5: The comparison between the direct drive in the left and the indirect drive (hohlraum) on the right side. [6]

The biggest institute where an inertial fusion is studied is National Ignition Facility (NIF) in Livermore, California.

The electrostatic confinement can be acquired using concentric spherical electrodes in vacuum; the positively charged particles are accelerated towards the middle of the inner anode, undergoing fusion if their energy is great enough. The devices working on this principle are called the Farnsworth–Hirsch fusors. The electrostatic confinement fusion is used in the tabletop neutron generators, employing DD or DT reactions.

Hydrogen bomb

Currently, the only fusion process mastered effectively is in the weapon industry. In the Teller–Ulam design, hydrogen bomb consists of primary part (fission bomb) and secondary part (fusion fuel coated in uranium with a plutonium spark plug) in reflective casing [7].

The process of explosion is shown in figure (1.6). The primary stage generates an intense flux of X–rays within hohlraum (bomb casing), which compress thermonuclear fuel by ablation and create conditions suitable for the fusion. The behaviour of Teller–Ulam devices is similar to the indirect laser–driven inertial fusion.

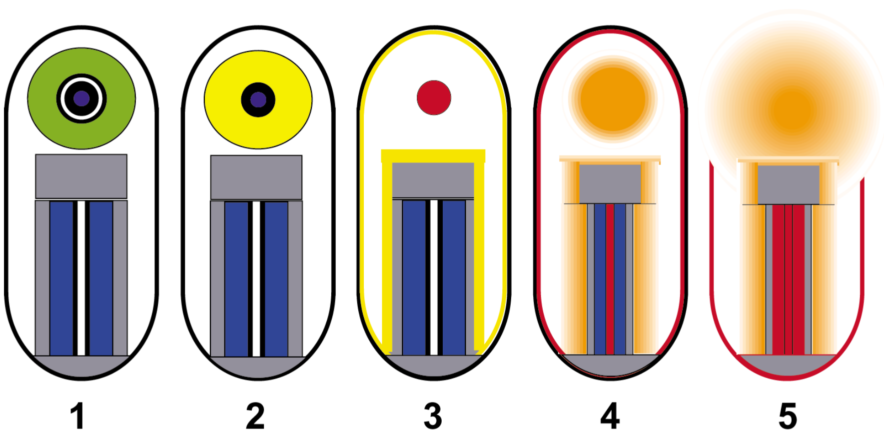

Figure 1.6: Triggering the fission in the primary stage, X–ray radiation is created in the shell. In the secondary stage, similarly to the hohlraum inertial fusion, X–rays compress fuel via ablation. After that, plutonium spark plug undergoes fission and heats the compressed secondary fusion fuel. At last, the uranium casing is fissioned by fusion neutrons to make additional yield. [8]

The largest thermonuclear bomb The Tsar Bomba (from Russain *Царь–бомба*) was tested on October 30th, 1961, yielding power of 50 to 58 megatons of trinitrotoluene (TNT), which corresponds to about $210 - 240$ PJ.

1.2.3 Magnetic Pinch

The pinching mechanism compresses plasma using high electric currents. The naturally occurring examples of this phenomena are solar flares and lighting; it can also be a result of a man–made experiment. There are three main types of pinches: z–pinch, θ–pinch and θ–z pinch. Those mentioned types differ in the direction in which the current is driven; z for axial, θ for azimuthal and θ–z for stabilised azimuthal (helical pinch). A difference between z and θ is shown in figure (1.7). The other widely used device for making a z–pinch is plasma focus, creating a hot dense column of plasma.

Among the largest research projects are Z Pulsed Power Facility at Sandia National Laboratory in Albuquerque, USA, Mather type dense plasma focus in Warsaw, Poland, and Filippov type dense plasma focus in Moscow, Russia.

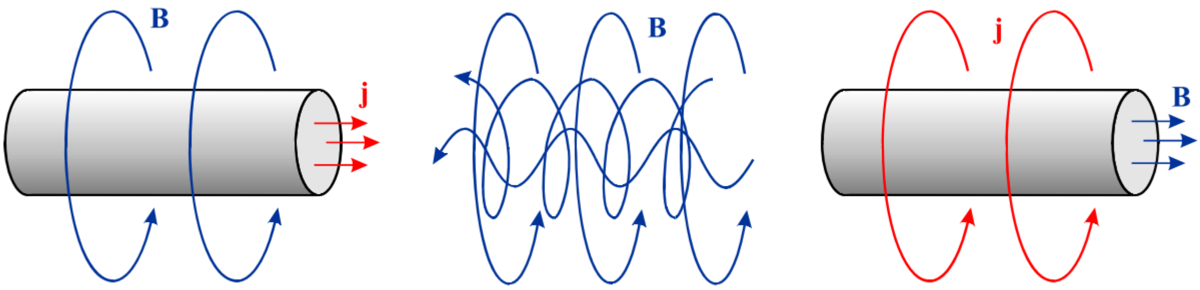

Figure 1.7: Difference between z– (left), θ–z (middle) and θ (right) pinch. In the z–pinch, the current is driven axially, in the θ–pinch azimuthally, an axial current is induced. θ–z pinch is a combination of those. [9]

Z–pinch

For research of fusion, the z–pinch is used as an imploding liner. It can be a system of wires, liquid bubble or gas in cylindrical shape. The energy stored in the capacitors is then discharged during a short period of time, causing the electric current I in the MA range and the magnetic field of induction $\mathbf{B}$ of the order of kT. The magnetic force $\mathbf{F}$ affecting the plasma thread of length vector $\mathbf{l}$ is

$$\mathrm{d}\mathbf{F} = I\mathrm{d}\mathbf{l} \times \mathbf{B}, \tag{1.2.2}$$

In case the magnetic p_m and the thermal pressure p_k are balanced

$$\frac{B^2}{2\mu} = nk_BT, \tag{1.2.3}$$

the pinch is in equilibrium [10]. This balance is essential for stable plasma, however, there are many instabilities and radiative processes which destroy this fragile equilibrium.

Z–pinches can also be used as a source of X–rays and neutrons, as a means of production of ultra–high pulsed magnetic fields. They can be even used to focus high–energy particles in accelerator experiments. [11]

1.2.4 Plasma focus

Using a coaxial configuration of electrodes, i.e. large anode in the center surrounded by smaller cathodes on the circular periphery, the ionized gas can be accelerated thus creating focused plasma on top of the anode. This process can be divided into three main phases as can be seen in figure (1.8).

There are two different construction types of plasma foci – Mather (USA) and Filippov (USSR). The difference between them is in the ratio of diameter d to length z of inner electrode. For Mather type, $d/z < 1$; for Filippov, $d/z > 1$ [11]. Nowadays, Mather type is used more often; the description of the discharge is below.

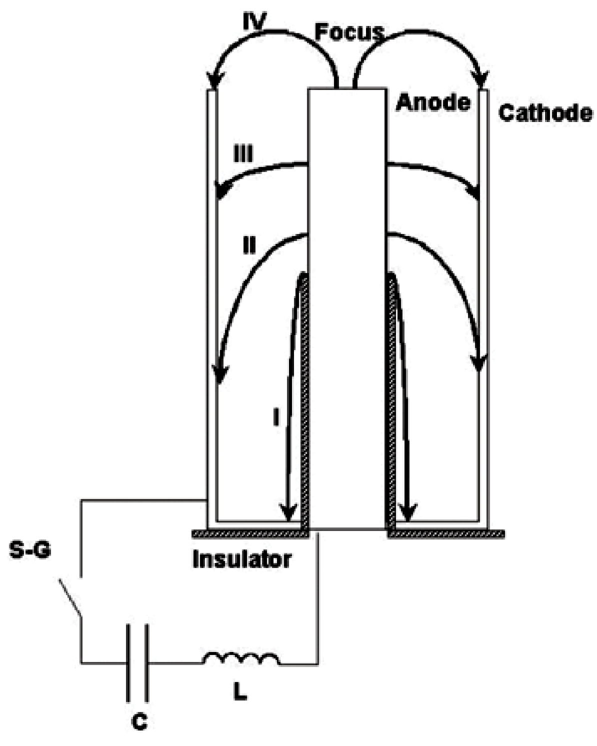

Figure 1.8: A scheme of a plasma focus with an equivalent electronic circuit. The capacitor C with charge $Q = C \cdot U$ is discharged via spark gap $\mathrm{S} - \mathrm{G}$. Discharge in gas begins over an insulator, continues accelerated to the top where is focused on the anode. [12]

I. Breakdown phase According to the Paschen's law, the breakdown voltage is a function of the pressure p and the gap distance d between the electrodes

$$V_b = \frac{Bpd}{\ln Apd - \ln\left(\ln\left(1 + 1/\gamma_{se}\right)\right)}, \tag{1.2.4}$$

where A, B are empirically measured constants dependent on the materials and γ_{se} is the secondary electron emission coefficient [13]. When this voltage is applied to

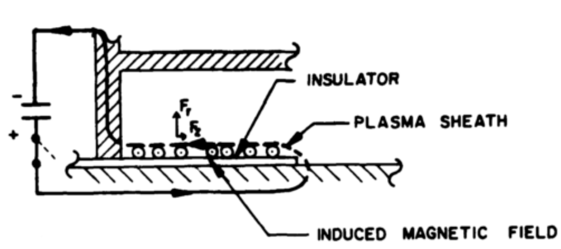

(a) Ionization of gas over an insulator, start of current flow.

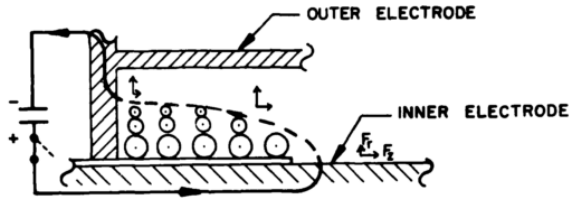

(b) Acceleration of plasma layer in radial direction via Lorentz force.

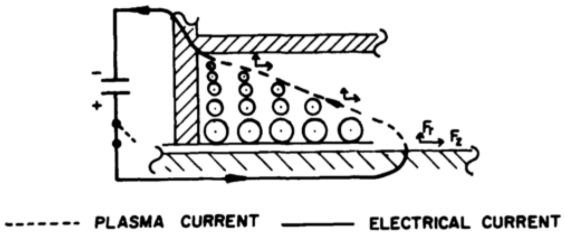

(c) Acceleration of plasma in axial direction.

Figure 1.9: Breakdown phase (inverse pinch effect) of plasma focus. [14]

the electrodes, the gas above the insulator is ionized. Current starts to flow through the created plasma layer, generating a magnetic field. Due to the Lorentz force, plasma is accelerated firstly in the radial direction to the cathodes, later when the discharge reaches anode, it is accelerated in the axial direction. This process is shown in figure (1.9), it is called the inverse pinch – the magnetic forces affect the plasma sheath to expand instead of pinch. [14].

II.–III. Acceleration phase Phase begins at the end of the breakdown phase, when plasma connects cathode and anode. The axial magnetic force $\mathbf{j_r} \times \mathbf{B}_\theta$ depends on the radius as $1/r$, therefore, the velocity of the plasma sheath is larger near the central anode. However, the accumulation of the plasma mass is non–linear: the mass build–up near the central electrode is linear, but drops in the direction towards the outer electrodes, where it is almost non–existent. This is called "snow–plow" effect, which slows down the movement of the central plasma sheath. [14]

IV. Collapse phase When leaving the conical arrangement of the electrodes, the plasma sheath is focused on the top of the anode. The compressed part of plasma then behaves in a similar fashion to z–pinch, generating X–rays and fusion neutrons, considering an application of the proper filling gas. The instabilities are also analogical.

Chapter 2

Plasma Instabilities

The biggest problems that occur during achieving thermonuclear fusion are plasma instabilities. Although plasma is able to remain in equilibrium for a short period of time, randomly occurring perturbations are likely to destroy it. In order to reach the desired experimental goals, the lifespan of plasma has to be extended by delaying the creation of the annihilating perturbations.

The easiest way to describe instabilities is in the case of a z–pinch, when the plasma is stable in Bennett equilibrium. Results from studying these instabilities can be generalized and taken into account in the other experiments and field configurations.

2.1 Bennett Equilibrium

The plasma is in steady–state equilibrium, when it is balanced and inert. Due to the cylindrical symmetry, for z-pinch this happens when

$$\nabla p = \mathbf{j} \times \mathbf{B}, \tag{2.1.1}$$

where p is pressure, $\mathbf{j}$ stands for the density of the electric current and $\mathbf{B}$ is magnetic induction. Using Ampere's law

$$\nabla \times \mathbf{B} = \mu_0 \mathbf{j} \tag{2.1.2}$$

in cylindrical coordinates for azimuthal magnetic field $\mathbf{B} = (0, B_\theta(r), 0)$ and axial current density $\mathbf{j} = (0, 0, j_z(r))$, the equilibrium condition can be rewritten from equation (2.1.1) as

$$\frac{\mathrm{d}}{\mathrm{d}r}\left(p_k + \frac{B_\theta^2}{2\mu_0}\right) + \frac{B_\theta^2}{\mu_0 r} = 0, \tag{2.1.3}$$

where p_k represents kinetic and $p_m = \frac{B_\theta^2}{2\mu_0}$ magnetic pressure, $p = p_k + p_m$. Term out of the derivation provides a radial confinement as a tension force generated by the curvature of the magnetic field, r representing the distance from the z–axis. [11]

Assuming an uniform current density $j_z = \frac{I}{\pi R^2}$ inside the plasma column with radius R, where I is electric current, the magnetic induction inside the column can be written as

$$B_\theta = \frac{\mu_0 I r}{2\pi R^2}. \tag{2.1.4}$$

Solving the differential equation (2.1.3) with considering the boundary conditions $p(R) = 0$ and neglecting the radiation from pinch, the pressure in the plasma column is

$$p(r) = \frac{\mu_0 I^2}{4\pi^2 R^2}\left(1 - \frac{r^2}{R^2}\right). \tag{2.1.5}$$

The condition for the current flowing through the plasma column when magnetic p_m and thermal pressure p_k are equal is called Bennett relation. Assuming the magnetic induction (2.1.4) for $r = R$ the pressure equality yields

$$I^2 = \frac{8\pi^3}{\mu_0} n_l k_B T, \tag{2.1.6}$$

where n_l is linear density of plasma.

2.2 Instabilities

The instabilities can be divided into two categories according to their origin:

- **Hydrodynamic** are caused by macroscopic motions of the plasma, i.e. an electron two–stream instability.

- **Kinetic** are based on interaction of specific particles with unstable mode, like ion acoustic-drift instability.

However, the first category is a more frequent subject of studies. [11]

The Hydrodynamic instabilities are focused on wave–like form of plasma flow. For the Bennett equilibrium, the wave solution depends on the distance from z–axis. Therefore, the perturbation of the static solution is

$$\psi(t, r, \varphi, z) = \psi_0(r) + \psi_1(r)\mathrm{e}^{\mathrm{i}m\theta + \mathrm{i}k_z z - \mathrm{i}\omega t}, \quad m = 0, \pm 1, \pm 2, \ldots \tag{2.2.1}$$

where $\psi_0(r)$ is the static solution, a disorder created from an aperiodic part $\psi_1(r)$, together with an oscillating exponential. Elements in the exponential are m modal number, θ azimuthal angle, k_z axial part of wave vector and ω angular frequency. [9]

In accordance to the modal number, plasma is unstable when

$$0 < m < \frac{2 - \beta}{1 - \beta}, \tag{2.2.2}$$

where $\beta = \frac{p_k}{p_m}$. For pinch plasma $\beta \ll 1$, therefore the only first two modes are relevant: $m = 0$ sausage and $m = 1$ kink instability. [15]

Another hydrodynamic instabilities occur on the surface where parts of plasma with different parameters meet: Rayleigh–Taylor or Diocotron instability.

2.2.1 Sausage Instability

The shape of this instability corresponds to the equation (2.2.1) for $m = 0$. The locations where plasma is compressed and expanded are repetitive, and the total volume is preserved.

Being dependant on $1/r$, the azimuthal component of magnetic field B_θ is different in every point along the z–axis. Therefore in places where plasma is expanded, B_θ is smaller and where plasma is compressed B_θ is larger than in equilibrium. This causes an additional compression and expansion caused by magnetic field. The name "sausage" is derived from its shape, shown in figure (2.1).

This instability can be reduced by applying an axial magnetic field B_z, i.e. creating θ–z pinch. Those field lines are frozen in plasma, creating a force opposing to the change.

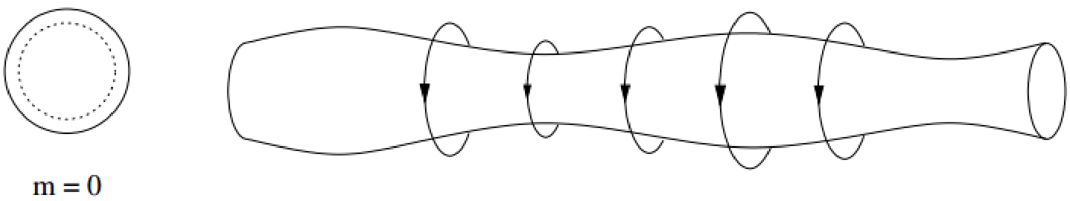

Figure 2.1: The physical form of sausage instability for z–pinch with cross–section where the dotted circle represents equilibrium. The magnetic field lines are represented by lines with arrows. [16]

2.2.2 Kink Instability

With $m = 1$ in the equation (2.2.1), the perturbation of the wave function results in the bending of the pinch. This bend causes the density of the lines of the magnetic field B_θ to get thicker on the concave and thinner on the convex side of the bend. As in the sausage instability, the arrangement of those lines enhances formation of the instability, creating kink, thence its name. It is shown in figure (2.2).

Using an additional axial magnetic field, the pinch becomes more stable due to the pressure which is reacting to the changes in the density of the azimuthal field.

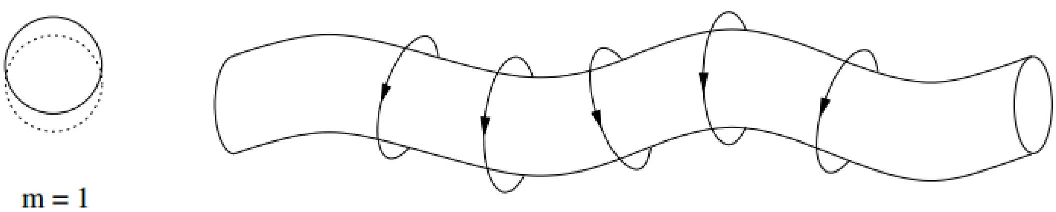

Figure 2.2: The physical form of kink instability for z–pinch with cross-section where the dotted circle represents equilibrium. The magnetic field lines are represented by lines with arrows. [16]

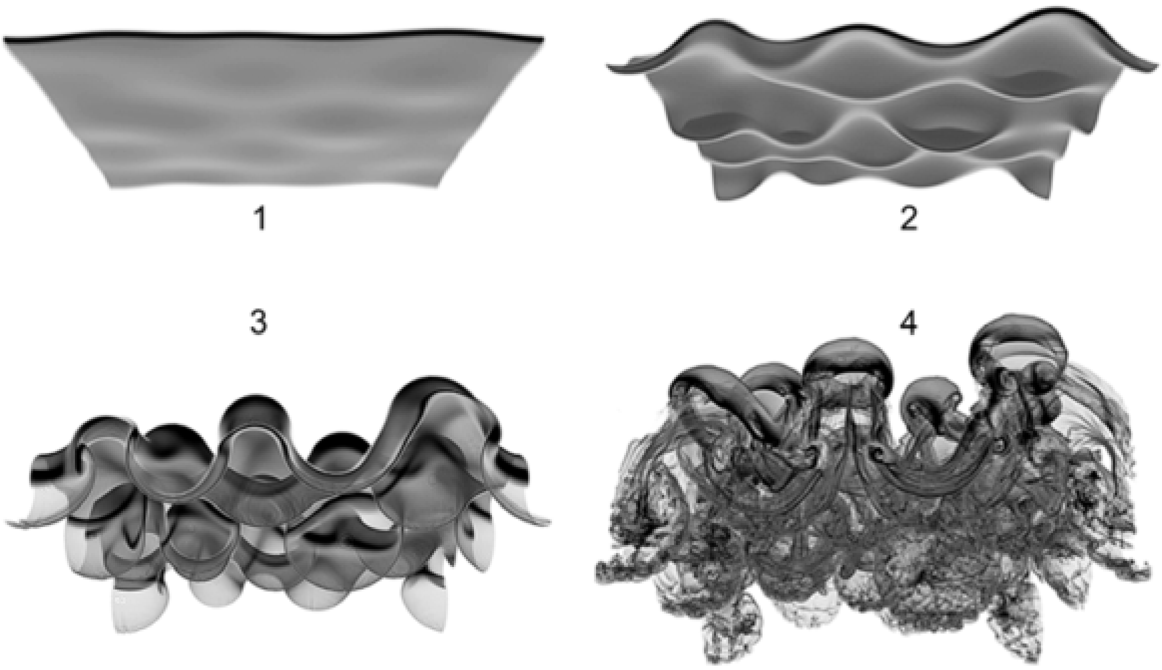

Figure 2.3: Numerical simulation of development of Rayleigh-Taylor instability. [9]

2.2.3 Rayleigh-Taylor Instability

This instability is generally created when a constant acceleration vector points in the direction from liquid with lower to a higher density. Those components are therefore mixing, trying to achieve state with lower energy, creating mushroom–like shapes as seen in figure (2.3). This effect can be also observed after an explosion of a nuclear bomb.

To prevent the creation of this instability, the experiment must be highly symmetrical. Applying a spin can also assist in suppression.

2.2.4 Diocotron Instability

It is plasma analogy of Kelvin–Helmholtz instability, where two layers are moving against each other, i.e. blowing wind over the water surface.

The separation of the charged particles in the radial direction can be caused by drifting or thermal radiation. Hence, the layers of plasma with different charges are created, causing a rotational movement. Its speed depends on the distance from the z–axis. [9] On the surface, the rotating thread meets the environment, creating swirls as seen in figure (2.4).

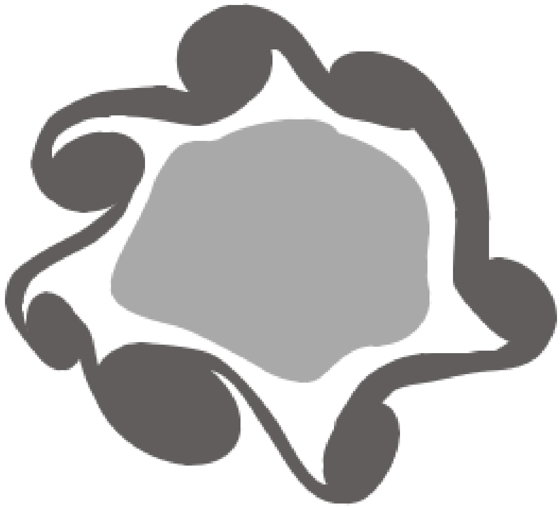

Figure 2.4: Cross–section of diocotron instability. [9]

2.3 Hotspots

In the initial phase of the plasma column collapse, hotspots – structures with high density and temperature, occur. At first, they were considered elements created by the sausage instability; however, this has since been disproved. Those spots emit hard X–rays, neutrons, nonthermal electrons and ions with energies from 20 keV to 1 MeV, they are always preceded by electron–beam–excited characteristic lines. [11]

In figure (2.5) a Schlieren photography of pinch of a wire in time is shown. The picture right represents the position of hotspots.

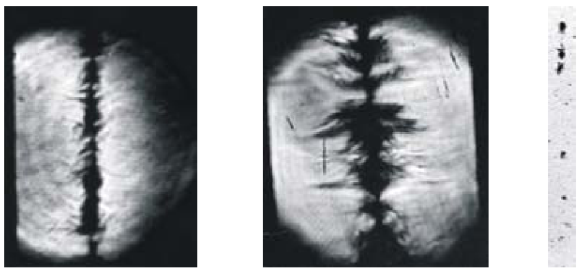

Figure 2.5: Schlieren photography of pinch of a wire with a diameter $r = 25$ μm, in times $t_1 = 14$ ns and $t_2 = 41$ ns, made in Imperial College in London, UK. In the right picture is an image of hotspots radiating in soft X–ray spectre. [10]

Chapter 3

Ionizing Radiation and Semiconductor Detectors

Ionizing radiation is defined as a particle radiation with energy sufficient to ionize atoms. It can be formed as a by–product of nuclear reactions, produced in particle accelerators or generated in X–ray tubes. Ionizing radiation can be divided into two basic categories:

- Direct ionization, i.e. electrons and heavy charged particles. They ionize surrounding atoms directly by Coulomb interaction.
- Indirect ionization with neutral hadrons such as neutrons and electromagnetic radiation, where secondary charged particles ionize the surrounding environment by a direct interaction.

Each of these types of ionizing radiation interacts differently with matter; therefore, several various detectors with unique characteristics have been created. Some of them are capable of detecting multiple types of incident particles.

3.1 Bethe–Bloch formula

Energy loss of heavy charged particles can be approximated by the Bethe–Bloch function. The specific energy loss is defined as a differential energy loss for the charged particles divided by a differential path length in material

$$S = -\frac{\mathrm{d}E}{\mathrm{d}x}. \tag{3.1.1}$$

The Bethe–Bloch formula calculates the stopping power as the mean value of equation (3.1.1), determined for heavy charged particles as

$$-\left\langle \frac{\mathrm{d}E}{\mathrm{d}x} \right\rangle = Kz^2 \frac{Z}{A} \frac{1}{\beta^2} \left[\frac{1}{2} \ln \frac{2m_e c^2 \beta^2 \gamma^2 W_{max}}{I^2} - \beta^2 - \frac{\delta(\beta\gamma)}{2} \right], \tag{3.1.2}$$

where z is charge of the incident particle, Z charge number of the medium, M mass of the incident particle, A atomic mass of the medium, I mean excitation energy of the medium, β ratio of speed of the particle v to the speed of light c, γ Lorentz factor, δ

density correction. W_{max} is the maximal energy transferred in a single collision, defined as

$$W_{max} = \frac{2m_e c^2 \beta^2 \gamma^2}{1 + 2\gamma\left(\frac{m_e}{M}\right) + \left(\frac{m_e}{M}\right)^2} \tag{3.1.3}$$

and K constant

$$K = 4\pi N_A r_e^2 c^2, \tag{3.1.4}$$

where m_e is electron mass, r_e classical electron radius, N_A Avogadro's number. Additional corrections are used for describing energy loss of electrons in matter.

Stopping power for copper as a function of $\beta\gamma$ can be seen in figure (3.1).

Energetic particles such as protons and deuterons from plasma focus have kinetic energies approximately 1 MeV, which corresponds to Anderson–Ziegler region.

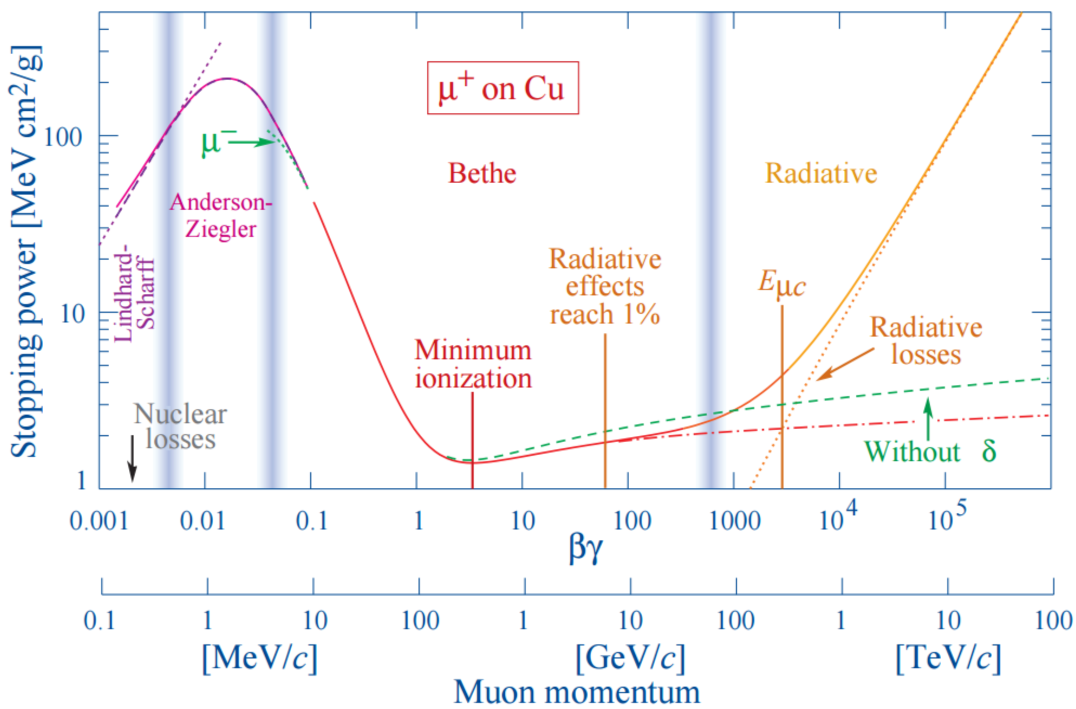

Figure 3.1: Stopping energy for muons in copper as a function of $\beta\gamma = p/Mc$. Bethe–Bloch formula (3.1.2) describes the mean rate of energy loss in the region $0.1 \lesssim \beta\gamma \lesssim 1000$. In the region below 0.1, shell and higher order corrections are applied, the dependency is experimentally measured and fitted. In the radiative region, $\mathrm{d}E/\mathrm{d}x$ is not a function of β and it is dependant on bremsstrahlung. [17]

3.1.1 Interaction of ionizing radiation

Particle detectors can only measure charged particles. Heavy charged particles and electrons interact primarily through Coulomb forces with electrons in the absorber, interactions with nuclei are rare. The incident particle is slowed down and electrons are accelerated, according to the law of conservation of momentum. Therefore, atoms in detector are ionized and pairs of electrons and positive ions or holes are created.

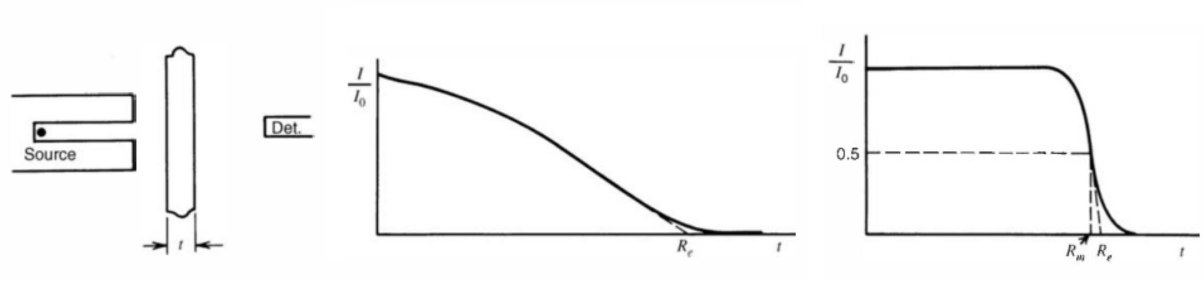

Figure 3.2: Comparison of ratio of number of detected particles I_0 without and I with absorbing medium of thickness t between electrons (middle) and alpha particles (right). The left picture represents design of such experiment. [18]

Having thousands of times larger mass than electrons, heavy charged particles ionize medium in the straight path. In comparison, incident electrons have large deviations in their path due to having the same mass as atomic electrons. This can be observed in figure (3.2), where ratio of number of detected particles with to particles without absorber decreases steadily for electrons, whereas it drops rapidly for heavy charged particles, as a function of thickness of the absorber.

In order to detect energetic photons or neutrons, the radiation must generally undergo catastrophic interaction – radically altering its properties. [18] For X– or gamma rays, it is a creation of secondary electrons, via the process of Compton scattering, photoelectric absorption or electron–positron pair creation, occurring at different energies. For neutrons, it is a creation of heavy charged particles, as a result of neutron–induced nuclear reactions or from gaining kinetic energy from collision. Products of these processes then interact as direct ionization mentioned above.

Photoelectric absorption

Incident photon undergoes an interaction with electron in atomic shell. Photon is absorbed and so called photoelectron is ejected from shell with kinetic energy E_{e^-}

$$E_{e^-} = h\nu - E_b, \tag{3.1.5}$$

where h is Planck constant, ν frequency of photon and E_b binding energy of electron. Therefore, photon must have energy greater than binding for reaction to occur.

Compton scattering

Incoming photon is deflected on an electron in the absorbing material, part of the energy is transferred. This results in the creation of a recoil electron and photon scattering angle θ, due to the conservation of energy and momentum. The energy of the scattered photon is calculated as

$$h\nu' = \frac{h\nu}{1 + \frac{h\nu}{m_0c^2}\left(1 - \cos(\theta)\right)}, \tag{3.1.6}$$

where h is Planck constant, ν is initial and ν' consequential frequency of photon, m_0c^2 is a rest–mass energy of electron. Since all scattering angles are possible, the energy range of secondary photons is also wide. [18]

Electron–positron pair creation

Having at least twice the rest–mass of electron $E_0 = 1.02$ MeV, energy of photon is converted into an electron–positron pair, all excess energy above this threshold is preserved as a kinetic energy of created particles. This reaction is more plausible for large energies of incoming photons of the order of MeV.

3.2 Detectors

Particle detectors can be made either from liquid, gas or solid materials. The material and method of construction determines energies and types of particles that can be detected. Currently used detectors are either gaseous ionization chambers, liquid detecting medium detectors and solid–state detectors.

Historically, bubble or cloud chambers have been used. They are created from liquid, which is kept just below the boiling point, or from a supersaturated vapour of water or alcohol. Charged particles transmit part of their energy to the molecules of medium, bringing liquid to the boiling point, or condensing water/alcohol. Therefore, path of their flight is visible, captured by photographic means. With addition of strong magnets, it is possible to measure momentum and charge from the curvature of the particle track.

3.2.1 Gaseous ionization detectors

In this type of detectors, ion pairs are created and detected in gas media. The energy needed for this ionization process depends on the construction of detectors, it is approximately 30 eV per ion pair. [18]

The created ion pairs will recombine quickly, therefore as a mean of prevention, external electric field is applied to the electrodes inside the chamber.

These detectors can be further divided into more specific groups. Impact of voltage on gas amplification factor and count rate for them is in figure (3.3).

Ionization chamber

They are gaseous equivalent to semiconductor detectors, operating at small voltages. Measuring created ionization current, the energy of incident particles can be determined.

Geiger–Müller tube

Applying high voltage, large electric field is achieved, creating avalanche of electrons from the incident particle. Geiger–Müller tubes therefore only work as counters of radiation–induced events, not as energy meters.

Proportional counter

Using combination of mechanisms of ionization chamber and Geiger–Müller tube, energy of the incident particle is measured. Input pulses are amplified via process of avalanche of electrons, however, a direct relation between measured and particle energy exists. Particles can be identified by measuring their charge, momentum and specific ionization loss.

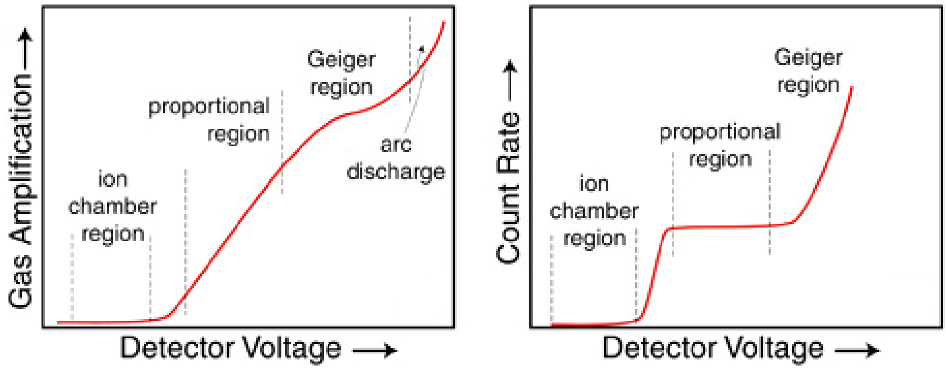

Figure 3.3: Effect of detector voltage on gas amplification factor and observed count rate for gaseous ionization detectors. [19]

3.2.2 Solid–state detectors

As the name suggests, these detectors are made of solid materials, in which the radiation interacts. In comparison to the previous group, the detection mainly occurs via creation of electron–hole pairs, which are similar to the ion pairs in gas. However, some types of solid–state detectors create visible light from the incident particle, which is then detected.

Solid–state detectors can be much smaller than gaseous ionization ones, due to a larger density of medium and therefore smaller distance which radiation must pass to lose most of its energy. Moreover, solid–state detectors have higher energy resolution and the amount of the energy required to create an electron–hole pair is about 10 times smaller than for the creation of an ion pair in the gas. For example, it is about 3.6 eV in the case of silicon. [18]

3.3 Semiconductor detectors

Semiconductor detectors are the most widely used type of the solid–state detectors. Silicon and germanium are mostly used due to their properties as elements of group 4 in periodic table. They are usually doped with donors (lithium, arsenic, phosphorus) or acceptors (boron, aluminium) of electrons, which create a $p-n$ junction. By diffusing dopants, the free charges around the junction disappear creating a depletion region – opposing another diffusion. It works as an active volume of the detector.

When incident particle passes through the detector, electron–hole pairs are created in the depletion region and move along the electric field lines between $p-$ and $n-$ doped areas, in the opposite directions. Those charges then arrive to the electrodes, where they are collected and measured. However, this signal would be small compared to the signal created by the thermally induced charge carriers. The probability of thermal creation of such pairs is given by

$$p(T) = CT^{3/2} \exp\left(-\frac{E_g}{2k_B T}\right), \tag{3.3.1}$$

where T is absolute temperature, k_B is Boltzmann constant and C is material constant. Bandgap energy E_g represents the difference of energies between the conduction band,

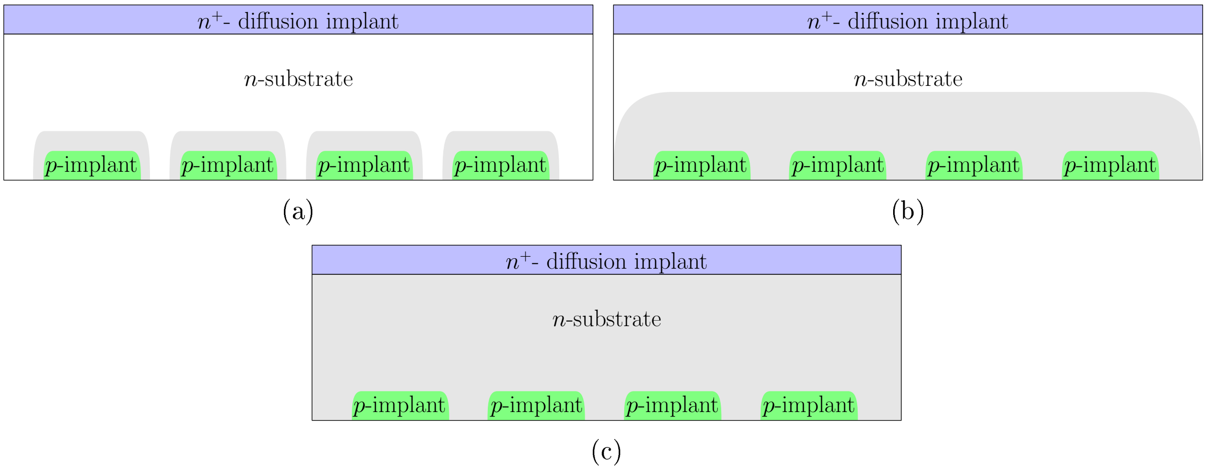

Figure 3.4: Widening of depletion region (shown as grey colour), from p to n implant, due to application of bias voltage.

in which electrons are free to migrate, and the valence band, where electrons are bound. For silicon and germanium, the value of the bandgap energy at the room temperature is $E_g = 1.115$ eV and $E_g = 0.665$ eV respectively. [18]

By lowering the temperature of the detector, or applying a reverse–bias voltage (the size of the depletion region is widened), the measured signal from the incident particles overwhelms the signal from the thermally created electron–hole pairs. Contrary to germanium, silicon detectors can be operated at room temperature. Thickness d of the depletion region is

$$d \cong \left(\frac{2\varepsilon U_b}{eN}\right)^{1/2}, \tag{3.3.2}$$

where ε is dielectric constant, U_b applied reverse–bias voltage, e elementary charge and N represents dopant concentration on the side of the junction that has lower dopant level. Thickness of the region is therefore proportional to $\sqrt{U_b}$. [18]

The configuration of implants which are connected to the readout of the sensor can differ. Either p^+ on n, where number of created holes is collected, or n^+ on p, which measures electrons. Despite this, the depletion region always starts over p and widens towards n, this process is shown in figure (3.4).

Semiconductor detectors can be used to detect either direct ionization or energetic photons. Calculated specific energy loss for charged particles, relevant for thermonuclear fusion, in silicon is shown in figure (3.5). Absorption coefficient of photons in silicon, according to their energy, is shown in figure (3.6).

There are two commonly used categories of semiconductor detectors which differ in size and geometry of sensitive elements – micro–strip and pixel detectors.

3.3.1 Micro–strip detectors

Segmenting $p-$doped implant into narrow strips, position of an incident particle can be measured in one direction. After an addition of another layer of such strips perpendicularly, the exact position of the impact can be determined. However, in this geometry,

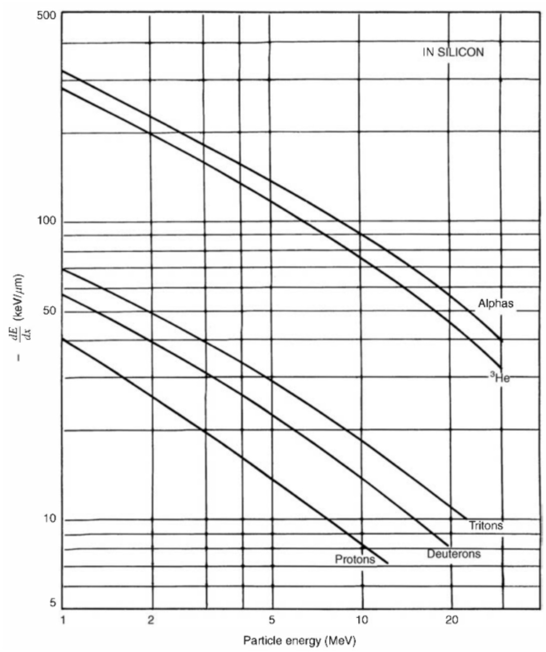

Figure 3.5: Specific energy loss calculated for different charged particles, significant for thermonuclear fusion, in silicon. [20]

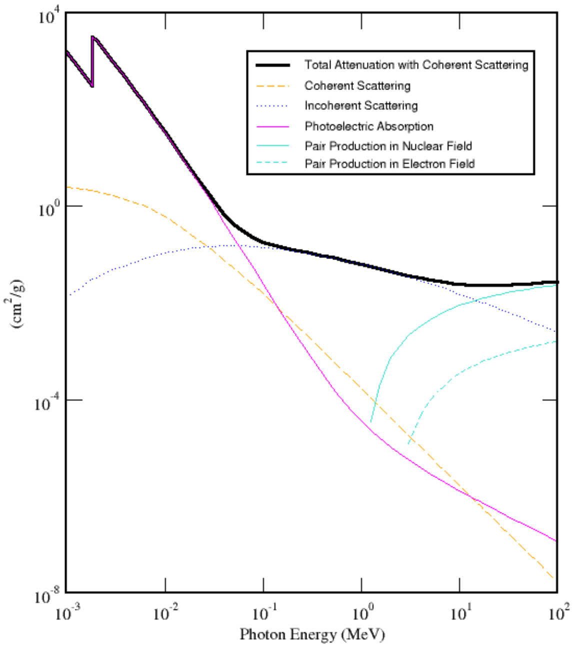

Figure 3.6: Mass attenuation coefficient for photons in silicon. Photoelectric absorption is dominant in the region to $\sim$ 0.05 MeV, from 0.05 to 10 MeV prevails Compton scattering and for energies above 10 MeV pair production in nuclear field dominates. [21]

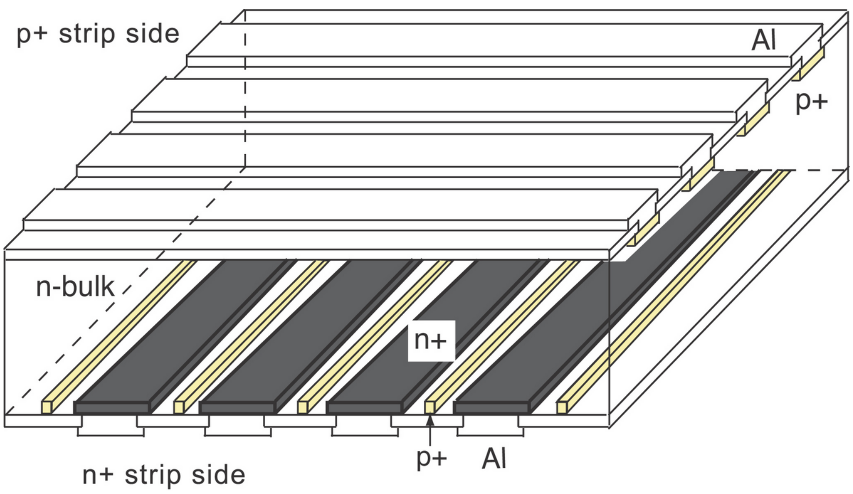

Figure 3.7: Cross–sectional view of double–sided silicon strip detector. Each n^+ strip is surrounded by p^+–doped implant, as a mean of isolation from adjacent strips. [22]

tracking ambiguities can arise. Moreover, at the same time the detector has to detect electrons and holes in the upper and lower strips respectively. Therefore this type of detector is not widely spread, its cross–section is shown in figure (3.7).

3.3.2 Pixel detectors

Instead of arranging implants to strips, pixel configuration is used for better hit position resolution. The pixel detectors can be further divided into two groups, depending on their construction.

Monolithic pixel detectors

Only one substrate is used, where both sensor and readout electronics are placed. Monolithic pixel detectors are very thin, with high efficiency, although difficult and costly to make. Cross-section is shown in figure (3.8a).

Hybrid pixel detectors

In comparison to the monolithic, the hybrid pixel detectors consist of two separate parts – readout electronics and sensor elements, connected by bump–bonds. This type of detectors can be cheaper to make, its cross–section shown in figure (3.8b). Medipix2 and Timepix detectors represent such construction.

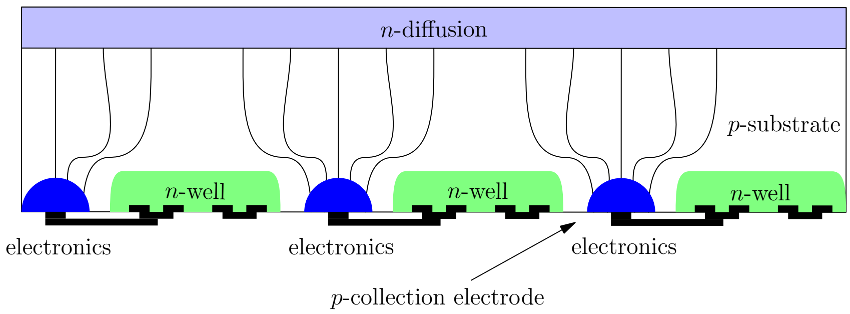

(a) Monolithic pixel detector.

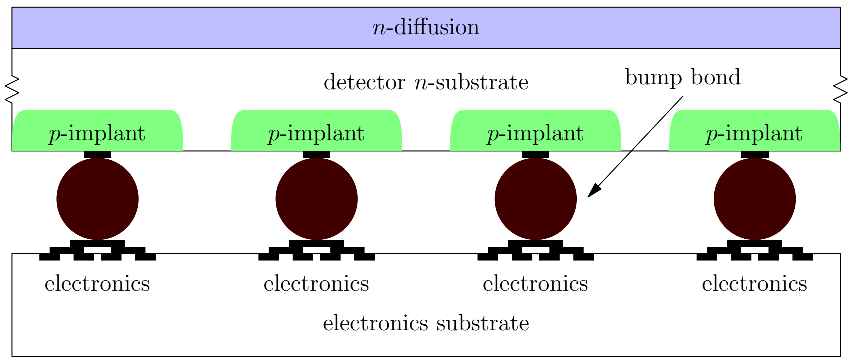

(b) Hybrid pixel detector.

Figure 3.8: Cross–sectional view of monolithic and hybrid pixel detector. [23]

Chapter 4

Apparatus

For the measurement presented in this thesis, PFZ-200 plasma focus with some of its diagnostics was used, together with Medipix2 and Timepix pixel detector. Monte–Carlo Simulation of particle–propagation through matter was also performed, to predict reliability of set–up and ability to detect photons from thermonuclear plasma.

4.1 PFZ-200

Plasma focus PFZ-200 is an experimental device located at the FEE CTU (Faculty of Electrical Engineering, Czech Technical University) in Prague. It is a small plasma focus, convenient for testing different electrode configurations, loads and diagnostic tools. [24]

4.1.1 Parameters

Schematics of the device is shown in figure (4.1). Configuration is of Mather type, with dimensions of the central electrode 2.5 cm in diameter and 11 cm in length. Electrode is made of CuW and is connected as an anode, an insulator is made of Al_2O_3. It reaches 35 mm from the bottom. Outer electrodes are from steel, 6 mm in diameter and 19 cm long. The experiment has 12 of these cathodes, coaxially arranged with diameter of cylindrical configuration 6 cm. Against the central anode with gap between $1-2$ cm an auxiliary Cu electrode with the diameter of 2.7 cm can be placed. This electrode supports pinching of the plasma, although during experiment auxiliary electrode was not used. [24]

The vacuum is made using turbo–molecular and rotary pump. The vacuum vessel is then filled with gaseous deuterium ${}^2_1$D at pressure in the range of $200-300$ Pa. Four capacitor banks have total stored energy 5.2 kJ and are charged to voltage $U_0 = 15$ kV, which allows maximal current in deuterium $I \approx 250$ kA, during 2 μs interval. The discharge occurs when air filled spark gap triggers. Shots can be repeated every 5 minutes.

4.1.2 Diagnostics

Many different methods are used for analysis of each shot. They can measure current, pressure or other parameters of plasma. However, for our experiment, the most important are visual interpretations. These are achieved using microchannel plate detector (MCP) and schlieren photography.

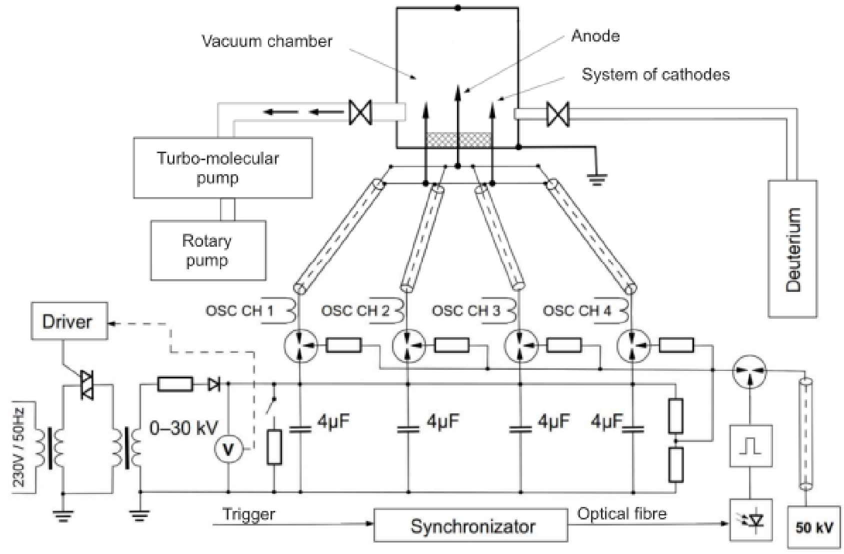

Figure 4.1: Scheme of plasma focus PFZ-200. [25]

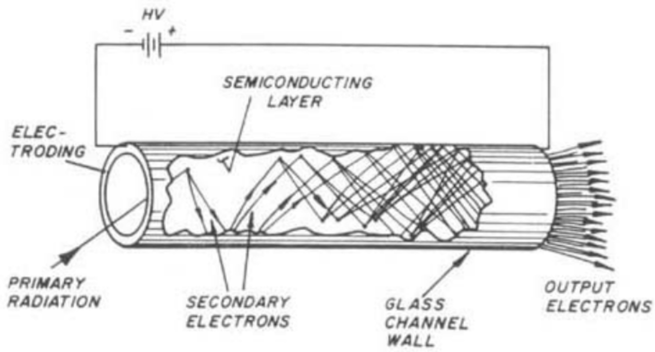

Figure 4.2: A straight channel electron multiplier. Avalanche of electrons gradually happens from incident photon. [26]

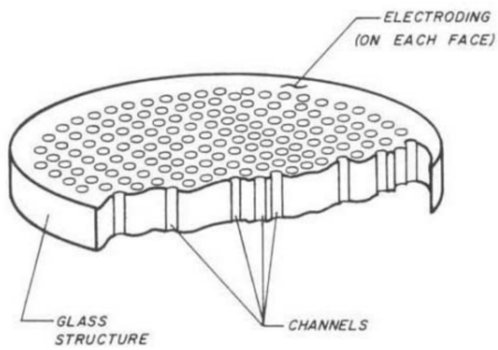

Figure 4.3: Microchannel plate created from number of straight channel electron multipliers. [26]

Microchannel plate detector

This type of detector is used to detect charged particles and energetic photons. It consists of a large number of channel electron multipliers where incident particles or photons create secondary electrons which are then multiplied. This process is shown in figure (4.2).

The individual channels are placed in a hexagonal pattern as is seen in figure (4.3). Dividing the active area into four parts and using power wires with different length, a time resolution can be achieved.

Schlieren photography

Schlieren (from German *schliere* – smear) photography is a method used for displaying changes in the gradient of the refractive index of medium. This can be used to display movements in the air. In plasma physics, when collimated laser beam passes through

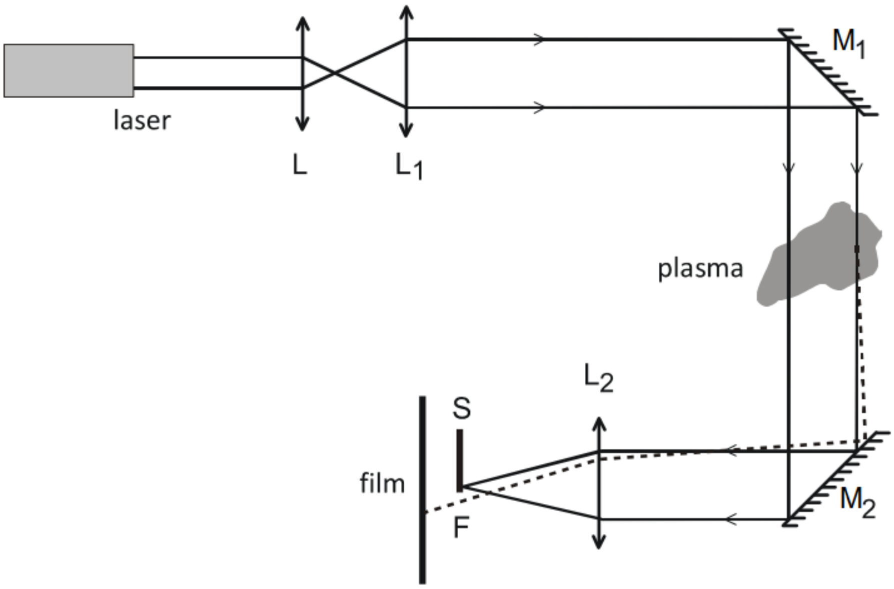

Figure 4.4: Principle of schlieren photography. Laser beam is widened, using set of lenses L and L_1. Normally, beam is then focused to the focal point F of lens L_2, exactly on edge of needle S. However, when in the path of the beam is non–zero gradient of refractive index caused by plasma, beam is shifted and it creates an image of this change on film. [9]

plasma, its path differs from the original path and is projected on a light–sensitive medium such as film. This process is shown in figure (4.4). The created picture then represents change of electron concentration.

4.2 Medipix2

Medipix2 is a hybrid pixel detector primarily designed for photon–counting X–ray imaging. It was developed in the European Organization for Nuclear Research CERN (from French *Conseil Européen pour la Recherche Nucléaire* - European Council for Nuclear Research). [27]

4.2.1 Parameters

The single chip has 256 × 256 pixels and is placed on chipboard 47 × 79 mm^2 large. Schematic picture of chipboard with dimensions is shown in figure (4.5a) and photography in figure (4.5b).

The chip dimensions are 16120 × 14111 μm^2 with an active area of 1.982 cm^2, corresponding to about 87% of the total chip area. Each one of 65536 pixels has size of 55 × 55 μm^2. Each pixel cell has 529 transistors.

The pixel structure can be divided into two blocks – analog and digital, as shown in figure (4.6). The analog part consists of pre-amplifier and two discriminators, which define local thresholds – boundaries of charge needed to be collected to accept particle hit. Digital part is responsible for control and counting number of detected particles.

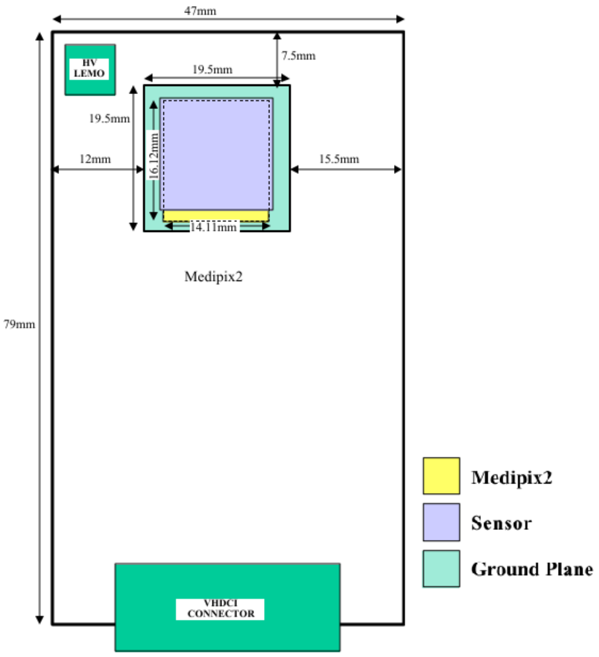

(a) Medipix2 schematic view with dimensions. [28]

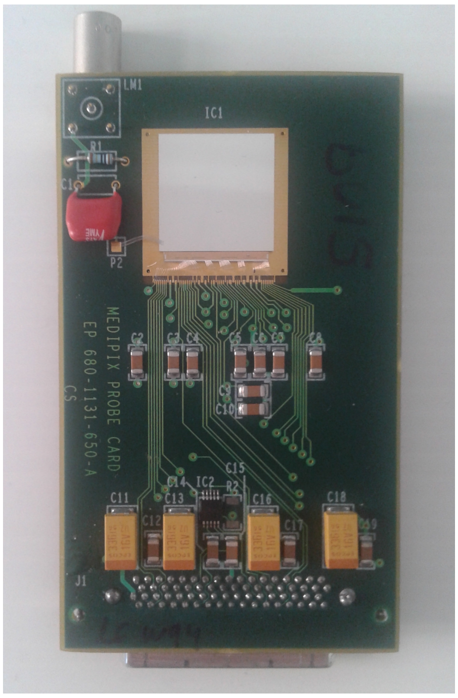

(b) Photography of Medipix2.

Figure 4.5: Schematic and real picture of Medipix2 chipboard.

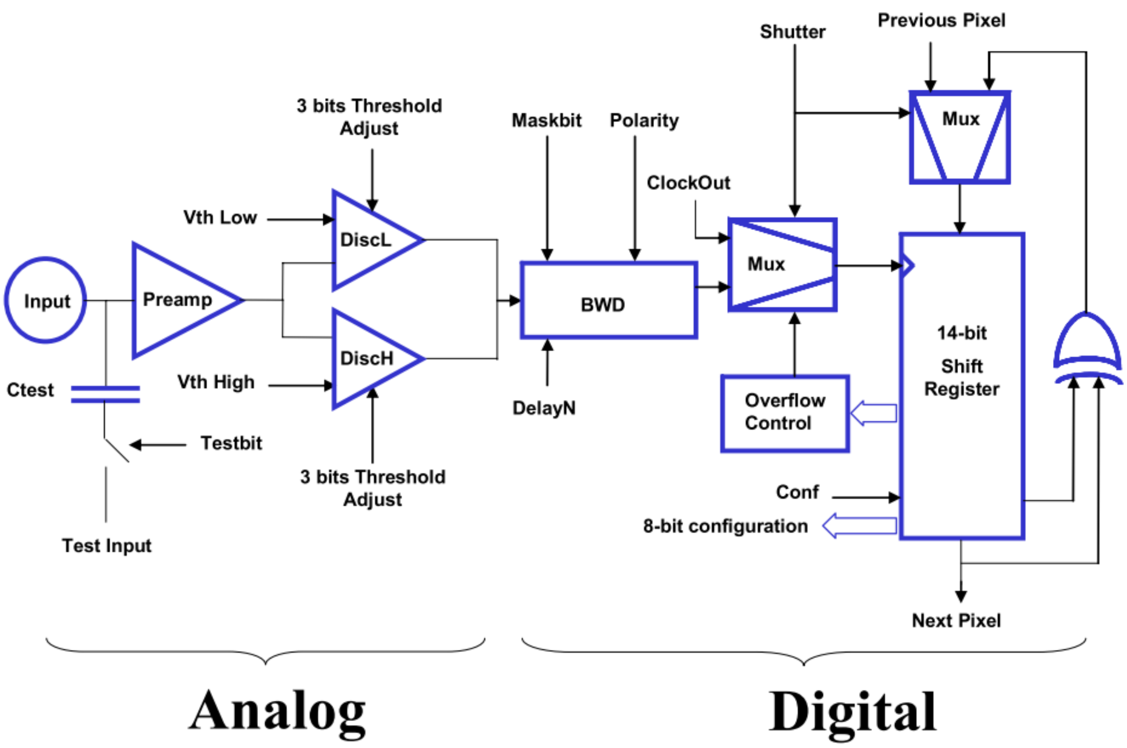

Figure 4.6: Medipix2 pixel cell blocks diagram. [27]

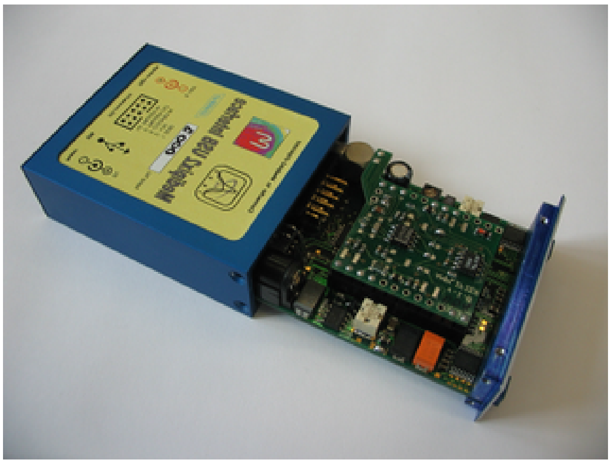

Figure 4.7: USB interface 1.0 used for communication between Medipix2/Timepix chip and computer.

As a mean to control electronics, 13 digital to analog converters (DAC) are used. They are responsible for setting bias voltage, currents and global threshold levels (THL, THH).

4.2.2 Readout

Several different methods for readout have been developed for Medipix2, which are essential for the communication between detector and computer. They provide method of adjusting DACs and also recording of measured data.

The most widely spread interfaces are Muros2 (Medipix2 Universal Readout System version 2) from NIKHEF (National Institute for Subatomic Physics) in Amsterdam and USB interface 1.0 from IEAP CTU (Institute of Experimental and Applied Physics, Czech Technical University) in Prague.

There is also number of programs used for communication, commonly used is Pixelman created by IEAP CTU in Prague.

USB interface 1.0

The main advantage of the USB interface is its small size $80 \times 50 \times 20$ mm^3 and portability. It is shown in figure (4.7). Power supply for both detector and interface is ensured via miniUSB cable, which also transfers data. Transfer speed is about 6 Mbit s^{-1}.

Pixelman

Pixelman is a program that serves for the control of sensor and data acquisition. It also enables calibration of the detector. Interface is shown in figure (4.8).

4.3 Timepix

Timepix chip is similar to Medipix2. Both use the same chipboard and readout software. Its main difference is, however, the capability to measure the energy by means of time over threshold, which allows certain determination of the energy of incident particles.

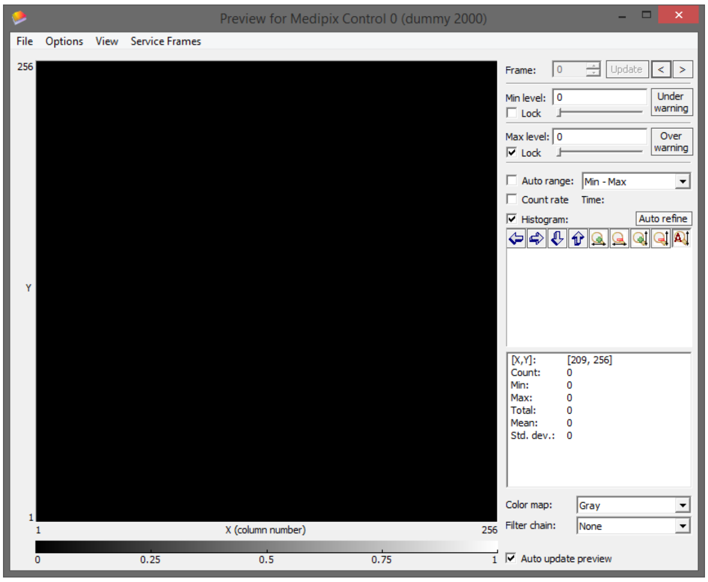

(a) Preview of device output.

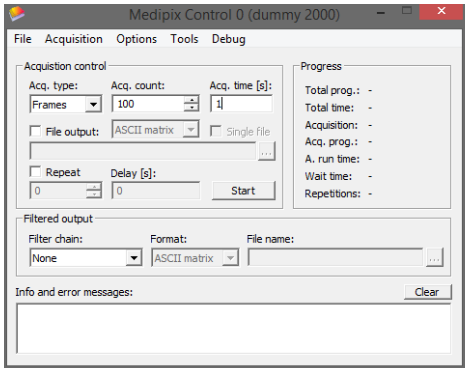

(b) Device control panel.

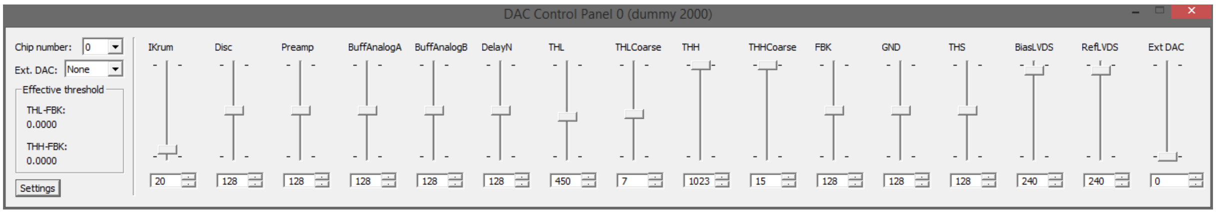

(c) DAC control panel with standard setting. Mainly used for changing low threshold (THL).

Figure 4.8: Pixelman interface.

4.4 Monte Carlo simulation

In physics, Monte Carlo simulations are used to predict behaviour of an experiment. It is important for successful creation of large projects such as particle detectors at the Large Hadron Collider (LHC) at CERN.

For simulating passage of particles through matter, Geant4 toolkit was created by worldwide Geant4 collaboration. [29]

4.4.1 Geant4

The toolkit is implemented in C++ programming language. It enables users to create experiment with specific geometry and materials, with possibility to detect particles. An event generator action then generates predefined particles with set energies and momenta. The type of interaction can be specified via physics list.

Different methods for output can be used. Geant4 has a variety of visualisations, depending on user preferences, which show trajectories of particles. Output from detector simulation can also be saved as a ROOT file.

Chapter 5

Results

The results of the work consist of simulation, construction of an apparatus for plasma properties measurement and measurement itself. In each of them, presented in this thesis, processes how it was accomplished and eventual interpretation of results are described.

5.1 Simulation

Before the start of the real experiment, a simulation of detector was needed to verify a proper detector operation in the expected range of energies. GEANT4 enables to simulate any material and record deposited energy in it.

In the work, simulation of Medipix2/Timepix sensor was made together with pinhole configuration which was later used in the measurement. Also, transmittances of aluminium and lead in large range of photon energies were simulated.

5.1.1 Parameters

The generation of events occurs in a specific region, which has to be predefined. For the purpose of this simulation, vacuum cubic area of volume $V = 1$ m^3 was created. Usage of vacuum both minimizes the risk of undesirable interactions and corresponds with the experimental set–up.

The Interaction of the incident particles with a matter are defined in the physics list, in this case it was Low Background Experiments (LBE), focusing on the electro–magnetic interactions. Because of this, low–energy photons were used in the simulation.

5.1.2 Set–up

Simulating the set–up for the measurement consisted of creating silicon sensor and obstacle from lead of thickness $d = 100$ μm, with pinhole of radius $r = 50$ μm. The sensor was divided into 256×256 boxes representing pixels, in which a number of hits and the deposited energy were recorded. Acquired data from the sensor were saved to a root file.

For a better demonstration of the operation, photons were generated from three points in triangular shape with two points at the bottom. They had an uniform distribution of the energy, from 10^0 to $2 \cdot 10^4$ eV. The square root of the uniform distribution was used for the vector of a movement direction in a conical shape. The directions were corrected so

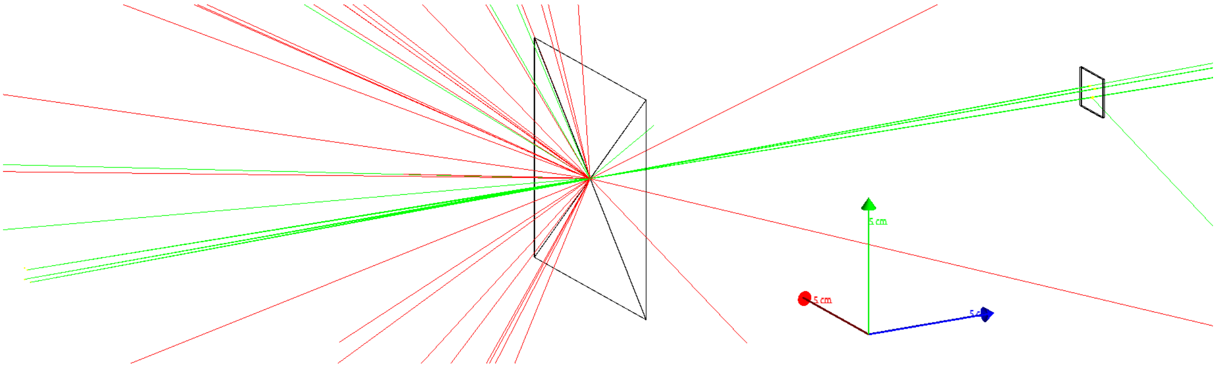

(a) Overview of the simulation set–up. Photons are shown green, electrons are shown red.

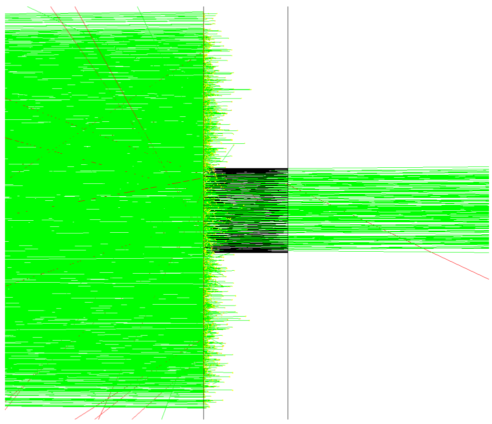

(b) Detailed view of the pinhole.

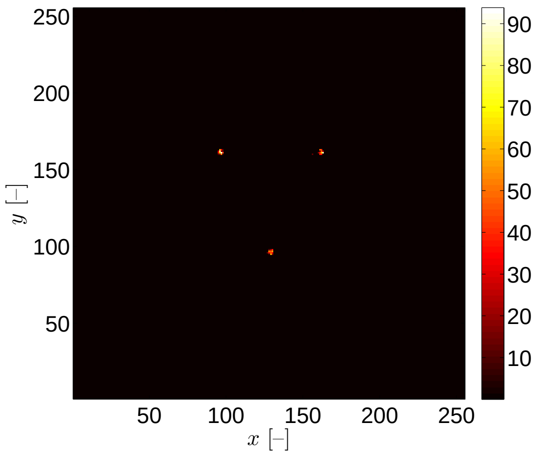

(c) Displayed data from sensor. Colorbar represents number of hits.

Figure 5.1: Simulation of photon transfer through pinhole from lead of thickness $d = 100$ μm and photon detection in silicon sensor, separated to 256×256 boxes representing pixels. Uniform distribution of energies with maximum $E = 20$ keV was used.

that the bases of the cones of radius $r' = 250$ μm at the pinhole were overlaying. The lead obstacle with the pinhole was right in the centre of the sensor and the particle sources. The number of generated photons for the simulation was $N = 1000$ from each vertex.

The simulation overview is shown in figure (5.1a). In figure (5.1b) are shown photon interactions in the lead obstacle with the pinhole. It is clearly visible that photons are stopped in lead and pass only through the pinhole, generating free electrons in material via Compton scattering. The matrix in figure (5.1c) represents the simulated sensor with detected photon numbers and positions. Reversion of the location of vertices on the sensor is evident.

5.1.3 Transmittance

The simulation of transmittance was done thrice, with slightly different parameters. Firstly, sensor without any obstacle was simulated, then sensor with lead of thickness $d = 100$ μm and finally with aluminium of thickness $d = 15$ μm.

Photons were used as the incident particle with a constant energy in range from 10^2 to

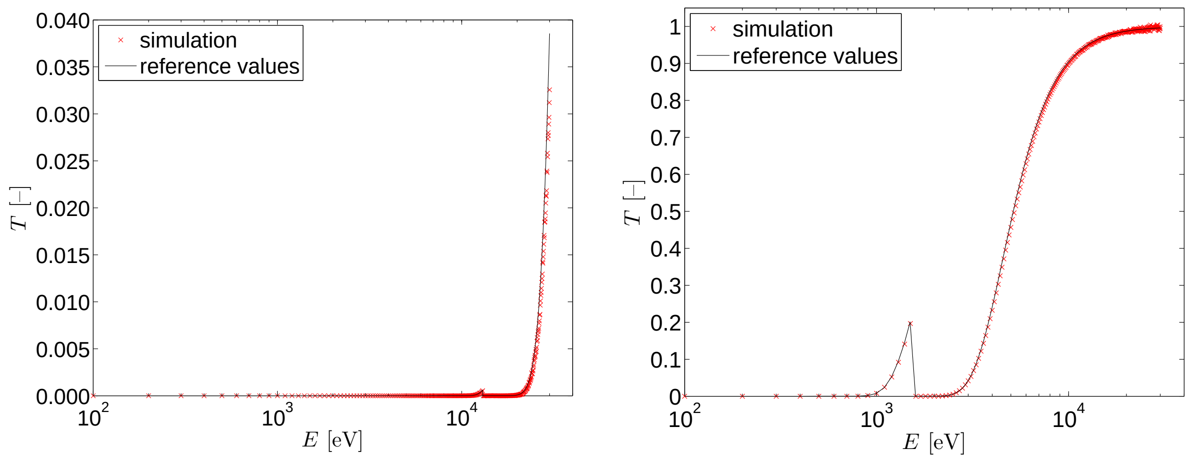

(a) Lead of thickness $d = 100$ μm.

(b) Aluminium of thickness $d = 15$ μm.

Figure 5.2: Simulated and real transmittance of lead and aluminium for photons with energies from 10^2 to $3 \cdot 10^4$ eV with step 10^2 eV [30]. Each simulated value represents 10^6 generated photons.

$3 \cdot 10^4$ eV with a step 10^2 eV. Theirs starting point was uniformly distributed in a circle of radius $r = 0.2$ mm, parallel to the sensor. The direction of movement was perpendicular to it. In the each run 10^6 photons were generated.

For obtaining the transmittance, the number of detected hits in the sensor with an obstacle was divided by the number of detected hits in the sensor alone. The division was due to the normalization of the output and it had to be done for each initial energy separately. The transmittance as a function of the photon energy is shown in figure (5.2), compared to the reference values.

The simulation data are corresponding well with the real values of the transmittance, only minor changes are visible at high energies.

5.2 Construction

The construction of the apparatus for measurement was performed in a number of attempts, each of them surpassing previous one in functionality. The main problem which occurred was the generation of strong electromagnetic interference (EMI) during discharge in spark gap or during generation of plasma.

Before the usage of both Medipix2 and Timepix, calibration of the thresholds was made, ensuring a proper performance of the detectors (via Pixelman interface: Device control panel). The bias voltage applied to the detectors was set to $U_b = 80$ V.

5.2.1 First attempt

Plasma focus PFZ–200 had a prepared port from straight vacuum tube and T–tube. Between them a pinhole of radius $r = 50$ μm from lead of thickness $d = 100$ μm was positioned. The usage of lead for the pinhole was convenient due to its opacity for photons in a large range of energies as shown in figure (5.2a). The necessity of T–tube was for pumping vacuum from behind the pinhole. The distance from the central anode to the

Figure 5.3: The Apparatus for the measurement with USB interface 1.0. It consists of Medipix2 detector in a vacuum sealable box and USB interface 1.0 in connected Faraday cage, together with an external battery and an USB to optical cable conversion. The components in the Faraday cage are connected via micro to double USB connector.

pinhole was set to $l_1 = 224$ mm, distance from it to the detector was $l_2 = 200$ mm.

Medipix2 pixel detector was prepared inside an aluminium alloy box which can be sealed and exhausted, shown in figure (5.3) on the left. It was then attached to a port on PFZ–200 plasma focus device and vacuum was created using rotary and turbo–molecular pump.

Using USB interface 1.0, Medipix2 was connected and powered. The detector was working as was confirmed using alpha and beta particle emitter. However, after trying a discharge in the spark gap, the detector stopped responding and displayed a strange pattern, shown in figure (5.4).

An effort was made to shield wires and USB interface 1.0 from EMI using thick aluminium foil and braided shielding. This was not working and same pattern was visible when discharging. Therefore, another method had to be devised.

5.2.2 Second attempt

Using the information from the first attempt, everything had to be enclosed in a Faraday cage. Both the detector and the readout together with a power source, the communication with PC had to be ensured via the USB/optical transceiver. The connection to the plasma focus was the same as in the first attempt. The final set–up is shown in figure (5.3). The Faraday cage was created using the same type of box as was used for the detector. In figure (5.5), the apparatus is connected to the PFZ-200.

After connecting Medipix2 box to the plasma focus and creating vacuum, the Faraday cage was connected and functioning of the device was tested. This configuration withstood EMI generated from the discharge in the spark gap, however, the moment the capacitors of PFZ–200 were being loaded, the detector stopped responding, repeating the noise pattern as in the first attempt.

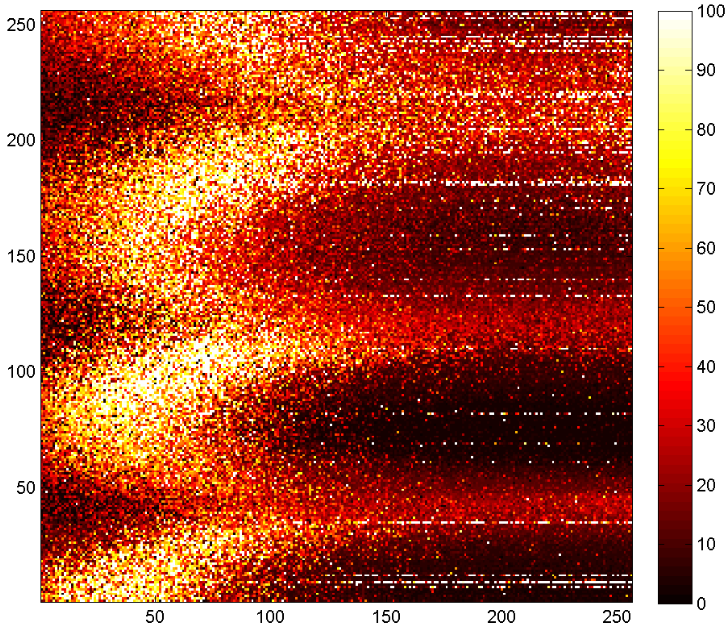

Figure 5.4: The pattern shown when the configuration of Medipix2 was lost and the detector stopped responding to USB interface 1.0 due to EMI. Colorbar represents the number of hits in the detector.

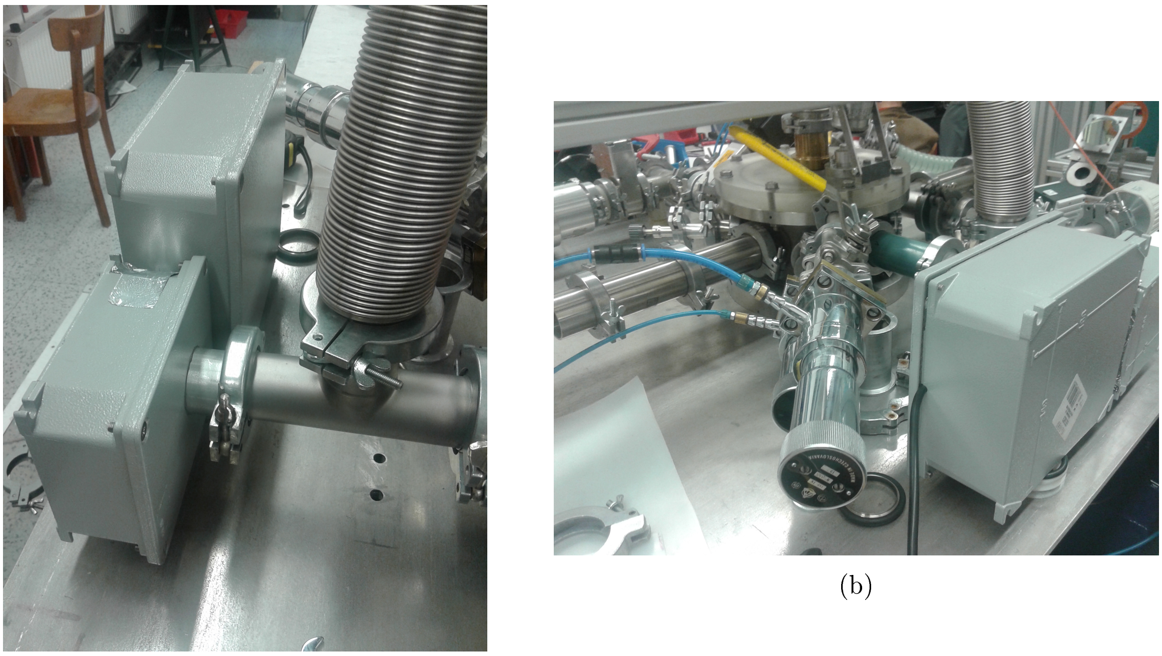

(a) (b)

Figure 5.5: The connection of Medipix2 apparatus to the plasma focus device, picture taken from two angles.

Figure 5.6: The apparatus for the measurement with Muros2. It consists of Medipix2 detector in the vacuum sealable box and USB interface 1.0 in connected Faraday cage, together with the external battery and the USB to optical cable conversion, used to control the bias voltage. In the large Faraday cage Muros2 is placed together with a computer, UPS and the other operating elements such as a keyboard, a mouse and a display.

It was discovered that the Faraday cage is not perfectly connected to the Medipix2 box thus it is not shielding EMI properly. This was fixed by scraping off paint on places which were suspected of a bad connection and by covering wire junction on Medipix2 box with a thick aluminium foil.

The operation of the device was tested and it was observed that Medipix2 was working properly, even after the discharge in the spark gap or after loading the capacitors. It was even possible to detect photons or particles from plasma.

5.2.3 Third attempt

Taking into account the results from the measurement with Medipix2, using Timepix would provide more useful information. The set–up created during the second attempt was functional, however, there was a problem with Timepix and USB interface 1.0 compatibility. Therefore, Muros2 had to be used.

The usage of Muros2 brought back problems with shielding, since conductive cables were connecting the equipment – large computer, Muros2 and Timepix in a box. Everything was put inside a large Faraday cage, however, wires were not shielded properly. This set–up is shown in figure (5.6). This resulted in the malfunction of Timepix, the same as in the first attempt with Medipix2.

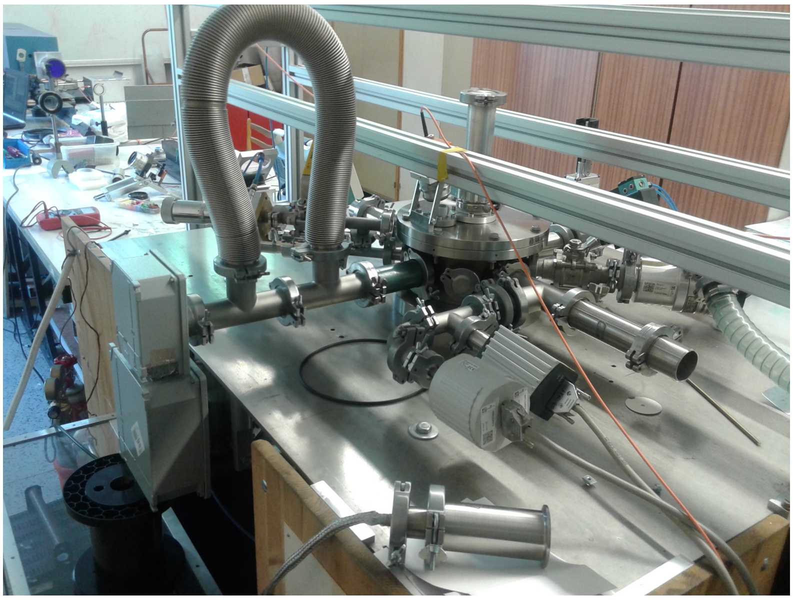

Figure 5.7: Connected Timepix apparatus to the plasma focus device.

5.2.4 Fourth attempt

The solution to problem with the third attempt was in updating firmware of USB interface 1.0. After that, Timepix was communicating and set–up from the second attempt was used for the measurement.

In addition, aluminium foil of thickness $d = 15$ μm was later added to pinhole as a filter for low–energy photons, as is clearly seen from figure (5.2b) where its transmittance of photons is shown. The distance from the central anode to it was also increased from $l_1 = 224$ mm to $l_1 = 307.5$ mm. This caused a minor difference in the connection of a bypass for vacuum and a rotation of the detector, as seen in figure (5.7).

5.3 Measurement

The data that were measured are divided into two categories depending on the used type of detector. The output files were in a form of matrices with 256×256 values, representing each pixel.

Medipix2 records were number of detected hits, for Timepix it was time over threshold. For a better visualisation, data from Timepix were normalized to the maximal detected value. Different rotations of the apparatus and pinhole image reversion were corrected using software, so as to correspond with the source. All imaging was done using MATLAB.

5.3.1 Medipix2

The measurement using Medipix2 was done with set–up made during the second attempt of the construction. The ratio of the distances from the central anode to the pinhole and from it to the detector causes that the size of the focused plasma displayed on Medipix was approximately 90 % of the original size.

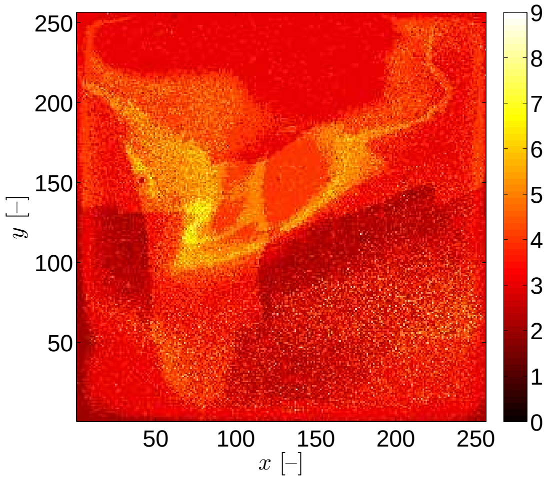

(a) THL = 355

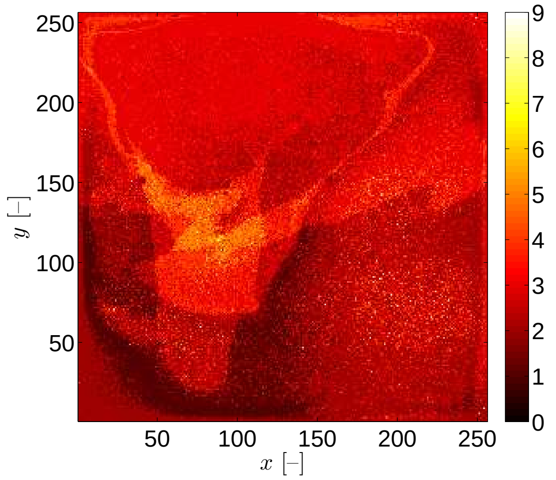

(b) THL = 320

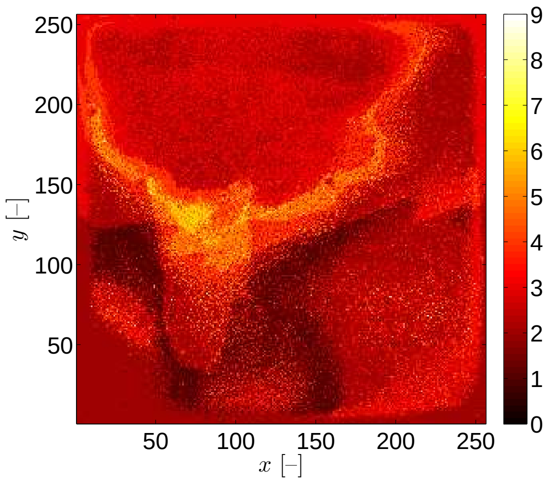

(c) THL = 280

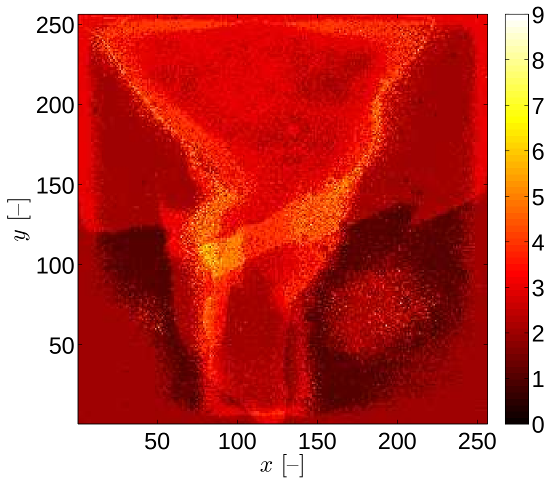

(d) THL = 240

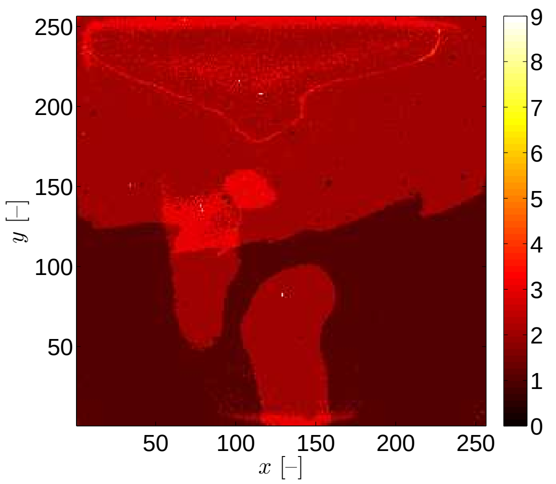

(e) THL = 200

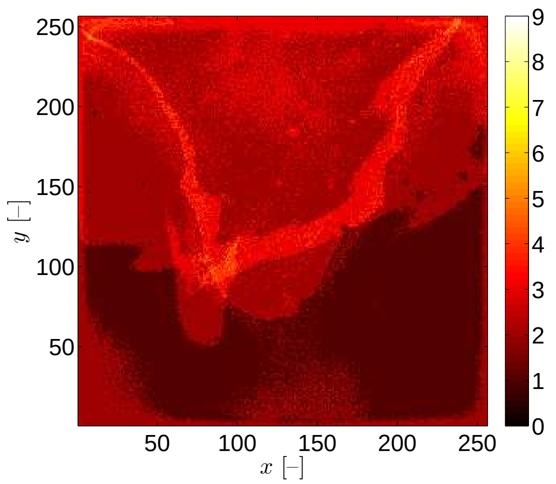

(f) THL = 200

Figure 5.8: Displayed data matrices of different shots from Medipix2 at various settings of THL. The colorbar represents the number of detector acquired hits. Bremsstrahlung and parasitic shapes are visible.

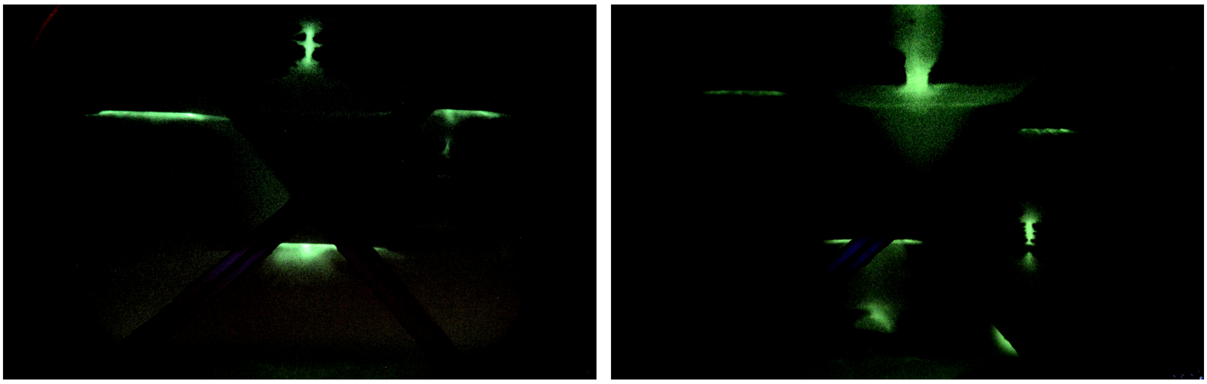

(a) (b)

Figure 5.9: Displayed data of the different shots from MCP. Evolution of z–pinch formation in time is visible, starting from the left and moving counter–clockwise.

Since the collapse phase and creation of z–pinch on plasma focus lasts for about 20 ns and Medipix2 is only able to detect particle hits during a fixed period of time, the exposition of $t = 1$ s was set. Due to this setting it was possible that the detector registered other radiation produced during the final stages of the discharge. Time needed to process and send detected hits in Medipix2 also causes an inability to detect whole duration of the discharge, therefore only one section of it is recorded.

During the experiments, the levels of THL were changed to separate low energy sources. The results from some of the measurements are shown in figure (5.8).

It is visible that the change in THL resulted in the increase of the contrast of the z–pinch. Circular objects in the left and the right lower corner, which are probably caused by X–ray radiation from the valves on the walls of the device, were also being dimmed.

In all of the pictures, two parasitic shapes are seen. One is occupying the upper half of the picture with a sawtooth bottom, the other is an elliptical shape near the middle on the left side. These two shapes are mostly visible in figures (5.8e) and (5.8f). They were probably created by a large number of the incoming particles and photons which saturated the detector. Despite that, the formation of plasma column is seen in all pictures.

From all of the measurements, only once was MCP triggered so that it captured a formation of z–pinch. It is shown in figure (5.9a), picturing the same event as Medipix2 in figure (5.8b). The images do not correspond well, which could be caused by the saturation of Medipix2.

5.3.2 Timepix

The measurement using Timepix was done using the set–up from the fourth attempt. It can be divided into two groups, depending on minor changes in the configuration.

First measurement

The first configuration was the same as in the measurement with Medipix2, only the detector was replaced with Timepix. Acquisition time was set to $t = 1$ s and the mode was set to time over threshold.

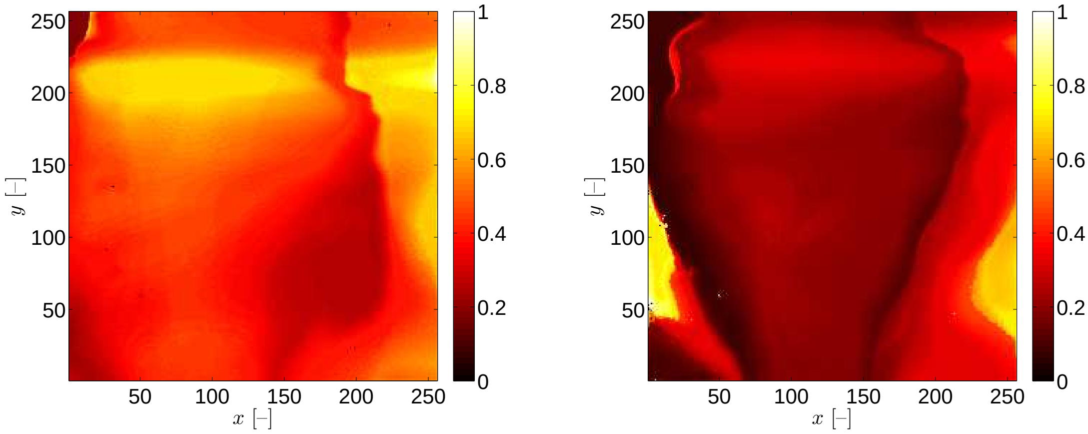

(a) THL = 260 (b) THL = 80

Figure 5.10: Displayed data matrices of different shots from Timepix first configuration at various settings of THL. The colorbar represents time over threshold of the detector acquired hits, normalized to the maximal value of each shot. Only vague shapes are visible.

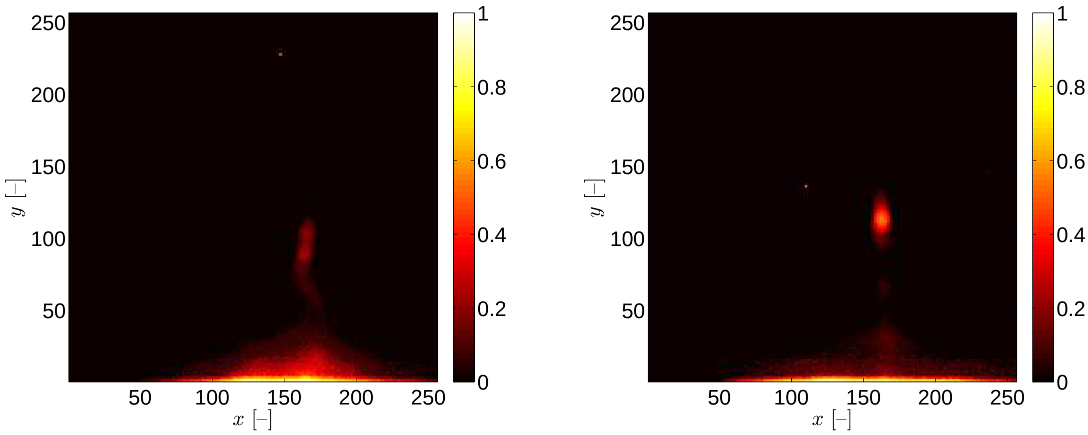

(a) THL = 150 (b) THL = 150

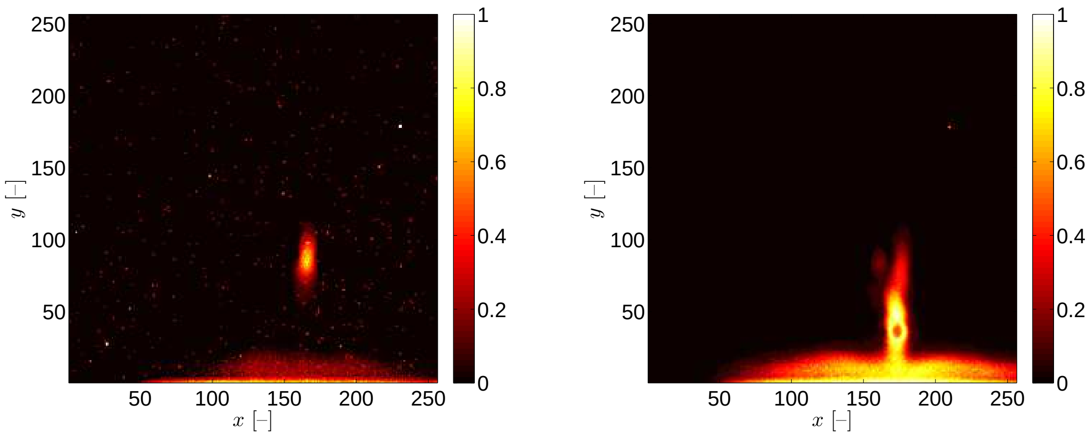

(c) THL = 100 (d) THL = 100

Figure 5.11: Displayed data matrices of different shots from Timepix second configuration at various settings of THL. The colorbar represents time over threshold of the detector acquired hits, normalized to the maximal value of each shot. The collapse phase of the plasma focus is visible.

The data obtained are displayed in figure (5.10). It is hard to specify any exact object or shape resembling z–pinch or its formation. This could be caused by the saturation of the detector by soft X–ray radiation where a quantity of photons hit the same pixel and deposited energy.

In an addition, the measurement in figure (5.10a) was captured by MCP, its output is shown in figure (5.9b). It is clear that there is no noticeable similarity between the two images.

Second measurement

As a second method of measuring with Timepix, the configuration was changed by an addition of an aluminium foil to the pinhole and elongation of a vacuum tube before it. The elongation caused shrinkage of the displayed area to approximately 65 % of the original size and also a rotation of set–up, due to the physical positioning and stability. Acquisition time was changed to $t = 2$ s

The data acquired from the measurement are shown in figure (5.11). The addition of the aluminium filter greatly improved the visualisation of the collapse phase of plasma focus, where pinching occurs. The oblong shape in the bottom part of the images is caused by hard X–rays radiated by the central anode where it was hit by the plasma column.

In all the pictures, z–pinch is clearly seen. Hints of instabilities are probably also visible in the measured data. The kink instability candidate is shown in figure (5.11a) and in figure (5.11b) is the sausage instability candidate.

Those measurements proved that it is possible to use such configuration to obtain reasonable results. However, the data could not be compared to the measurement from MCP, due to technical difficulties with the device.

The comparison to an another mean of imaging is crucial for the proper interpretation of the results. Also, more measurements at more threshold levels have to be done for a better statistical relevancy. Another essential factor is a calibration of the thresholds using an uniform energy source with known energy, since without that only a comparison of the detected energies is possible.

Conclusions

This thesis is focused on designing a new method of plasma diagnostics using semiconductor pixel detectors. Brief introduction to plasma physics and experiments is covered in the first chapter. A description of plasma generating devices working on the principles of magnetic or inertial confinement is given, focusing mainly on the z–pinches and plasma foci as they are of particular interest in this thesis. The second chapter deals with types and characteristics of plasma instabilities. Relevant information about ionizing radiation is provided in the third chapter, along with general properties of detectors. The principles of semiconductor detectors are examined in more details.

The fourth and fifth chapters are dedicated to the experimental setup and the performance of the measurement. These chapters represent author's personal contribution to the studied subject. The fourth chapter provides the description of PFZ-200 plasma focus and its optical diagnostics systems. This includes the characteristics of Medipix2 and Timepix detectors their readout interface and controlling program, as these are the main components of the new diagnostic method. The process of creating a new diagnostic method consisted of simulation, construction of an apparatus for plasma properties measurement and measurement itself. All of these are mentioned in the final chapter.

A dedicated simulation has been created to model the behaviour of the experimental set–up. The apparatus consists of: a source of particles, a lead obstacle with a pinhole and a sensor. This is shown schematically in figure (5.1). Another simulation is used to investigate the dependence of transmittance of lead and aluminium on the energy of photons. The simulation results are compared with reference values obtained from [30] as is shown in figure (5.2).

The construction of the operating apparatus was done in multiple development steps. The detector was embedded inside an aluminium box which was attached to the port on the plasma focus. A pinhole in the leaded plate was made between the detector and the central anode of PFZ-200. The first challenge was to address the electromagnetic interferences which interrupted communication between Medipix2 and USB interface 1.0. The solution was in enclosing the readout and the detector in a Faraday cage and transferring the signal via optical cable. With this successful adjustment to the set–up, both Medipix2 and Timepix were able to collect data from the plasma focus.

Three different sets of data were obtained. The records made by Medipix2 are clearly noisy with several visible parasitic shapes as shown in figure (5.8). Henceforth, Timepix was proposed as a better choice, since it allows to compare deposited energy. However, minor difficulties occurred during the first attempt of acquiring data. The detector was probably saturated by the low–energetic photons which caused formation of indifferent shapes, see figure (5.10). It should also be noted that these shapes bear little resemblance to the images made by microchannel plate as shown in figure (5.9).

The final set of data was obtained from Timepix after placing a thin aluminium foil directly above the pinhole. From the simulation mentioned above, the transmittance of this foil would decrease the number of soft X–rays. This is confirmed by the results of the measurement shown in figure (5.11). Here, the structure resembling the z–pinch created plasma column is visible together with a few instability candidates.

To summarize, the possibility of using semiconductor pixel detectors as a method of diagnosing plasma allows for the development of new measurement strategies. However, for better interpretation of the results it is recommended to compare to another type of diagnostics, e.g. microchannel plate or Schlieren photography. Calibration and specification of thresholds should be considered an important factor.

Bibliography

[1] BP p.l.c.: **BP Statistical Review of World Energy June 2015** [online]. 64th ed. London [cit. July 14., 2015]. Available at:
http://www.bp.com/content/dam/bp/pdf/Energy-economics/statistical-review-2015/bp-statistical-review-of-world-energy-2015-primary-energy-section.pdf

[2] Planck collaboration: **Planck 2015 results. XIII. Cosmological parameters**. Astronomy & Astrophysics [online], in press, 2015, 67 p.
http://xxx.lanl.gov/abs/1502.01589v2

[3] Wikimedia Commons - Shared media repository: **Binding energy curve - common isotopes** [online]. Wikimedia Foundation [cit. January 2., 2015]. Available at:
https://upload.wikimedia.org/wikipedia/commons/archive/5/53/20120808130831%21Binding_energy_curve_-_common_isotopes.svg

[4] Coraddu M., et al: **Thermal distributions in stellar plasmas, nuclear reactions and solar neutrinos**. Brazilian Journal of Physics [online], vol. 29, no. 1, 1999, p. 153-168, ISSN 0103-9733.
http://dx.doi.org/10.1590/S0103-97331999000100014

[5] National Physical Laboratory, Kaye&Laby: **Tables of Physical & Chemical Constant**, Chapter 4, Section 4.7, Subsect. 4.7.4 Nuclear Fusion. [online], [cit. April 4., 2015]. Available at:
http://www.kayelaby.npl.co.uk/atomic_and_nuclear_physics/4_7/4_7_4.html

[6] Boyd T. J. M., Sanderson J. J.: **The Physics of Plasmas**. Cambridge university press, New York, 2003, p. 548, ISBN 978-0-521-45290-5.

[7] Sublette C.: **Nuclear Weapons Frequently Asked Questions** [online], [cit. March 3., 2015]. Available at:
http://www.nuclearweaponarchive.org/Nwfaq/Nfaq4-4.html#Nfaq4.4

[8] Rohlena K.: **Inerciální fúze**. Československý časopis pro fyziku, vol. 60, no. 6, 2010, p. 346-360, ISSN 1361-6587.

[9] Kulhánek P.: **Úvod do teorie plazmatu**. AGA, Prague, 2014, 388 p., ISBN 978-80-904582-2-2.

[10] P. Kubeš. **Impulsní silnoproudé výboje a jejich diagnostika**. FEL, Prague, 2004, 83 p.

[11] Liberman M. A., de Groot J. S., Toor A., Spielman R. B.: **Physics Of High-Density Z-Pinch Plasmas**. Springer, New York, 1999, 285 p., ISBN 978-1-4612-7138-3.

[12] L. Soto et al. **Research on pinch plasma focus devices of hundred of kilojoules to tens of joules**. Brazilian Journal of Physics [online], vol. 34, no. 4B, 2004, p. 1814-1821.
http://dx.doi.org/10.1590/S0103-97332004000800054

[13] Liberman M. A., Lichtenberg A. J.: **Principles of Plasma Discharges and Materials Processing**. 2nd ed. John Wiley & Sons, Hoboken, N.J., 2005, 794 p., ISBN 978-0-471-72001-1.

[14] Willenborg D. L., Hendricks C. D.: **Design and Construction of a Dense Plasma Focus Device**. University of Illinois, Department of electrical engineering, Urbana, 1976, 97 p.

[15] Miyamoto K.: **Fundamentals of Plasma Physics and Controlled Fusion**. 3rd ed. National Institute for Fusion Science, Toki, 2011, 360 p.

[16] Braithwaite J.: **The stability of toroidal fields in stars**. Astronomy & Astrophysics [online], vol. 453, no. 2, 2006, p. 687-698.
http://dx.doi.org/10.1051/0004-6361:20041282

[17] Olive K. A., et al (Particle Data Group): **Review of Particle Physics**. Chinese Physics C, vol. 38, no. 9, 2014, 1676 p.
http://dx.doi.org/10.1088/1674-1137/38/9/090001

[18] Knoll G. F.: **Radiation Detection and Measurement**. 4th ed. John Wiley & Sons, New York, 2010, 860 p., ISBN 978-0-470-13148-0.

[19] Wittke J. H.: **Wavelength Dispersive Spectrometry** [online]. North Arizona University, 2008 [cit. March 21, 2015]. Available at:
http://www4.nau.edu/microanalysis/microprobe-sem/signal_detection.html

[20] Skyrme D. J.: **The passage of charged particles through silicon**. Nuclear Instruments and Methods, vol. 57, 1967, p. 61-73, ISSN 0029-554X.
http://dx.doi.org/10.1016/0029-554X(67)90498-3

[21] Berger M. J., et al: **XCOM: Photon Cross Sections Database** [online]. NIST, 2010 [cit. April 11, 2015]. Available at:
http://www.nist.gov/pml/data/xcom/

[22] Takeda S.: **Double-sided silicon strip detector for x-ray imaging** [online]. SPIE, 2008, 3 p. [cit. March 31, 2015]. Available at:
http://spie.org/documents/Newsroom/Imported/0889/0889-2008-05-15.pdf

[23] Hejtmánek M.: **Development of Novel Silicon Particle Detectors** Diploma thesis, Czech Technical University in Prague, 2010, 56 p.

[24] Kubes P., et al: **Research of the Small Plasma Focus with an Auxiliary Electrode at Deuterium Filling** Plasma Physics Reports, vol. 35, no. 10, 2009, p. 824-827, ISSN 1063-780X.
http://dx.doi.org/10.1134/S1063780X09100031

[25] Šíla O.: **Energetické spektrum neutronů z reakce D-D v plazmatickém fokusu** Diploma thesis, Czech Technical University in Prague, 2010, 111 p.

[26] Wiza J.L.: **Microchannel plate detectors** Nuclear Instruments and Methods, vol. 162, no. 1, 1979, p. 587-601, ISSN 0029-554X.
http://dx.doi.org/10.1016/0029-554X(79)90734-1

[27] Llopart X.: **MPIX2MXR20 Manual v2.3** [online]. CERN [cit. April 10., 2015]. Available at:
http://medipix.web.cern.ch/medipix/protected/medipix2/medipix2_download.php?file=files%2FMpix2MXR20+Documentv2.3.pdf

[28] Medipix collaboration: **CERN Single Chip Board Dimensions** [online]. CERN [cit. April 10., 2015]. Available at:
http://medipix.web.cern.ch/medipix/protected/medipix2/medipix2_download.php?file=files%2FPCB_dim.pdf

[29] Geant4 collaboration: **Geant4 — a simulation toolkit** Nuclear Instruments and Methods, vol. 506, no. 3, 2003, p. 250-303, ISSN 0168-9002.
http://dx.doi.org/10.1016/S0168-9002(03)01368-8

[30] Henke B.L., Gullikson E.M., Davis J.C.: **X-ray interactions: photoabsorption, scattering, transmission, and reflection at E=50-30000 eV, Z=1-92** Atomic Data and Nuclear Data Tables, vol. 54, no. 2, 1993, p. 181-342.
http://dx.doi.org/10.1006/adnd.1993.1013